JGR Planets

RESEARCH ARTICLE
10.1029/2019JE006196

Key Points:
- We identified 64 paleolakes in the northwest Hellas region and investigated their geomorphology, age, and mineralogy in detail
- Paleolakes drained in the early Hesperian and were extensively resurfaced by volcanic and glacial activity at ~3.3 and ~0.9 Ga, respectively
- A climate transition from warm and wet to semi-arid then to cold and dry happened in the study region from the Noachian to the Hesperian

Supporting Information:
- Figure S1

Correspondence to:
L. Xiao,
longxiao@cug.edu.cn

Citation:
Zhao, J., Xiao, L., & Glotch, T. D. (2020). Paleolakes in the northwest Hellas region, Mars: Implications for the regional geologic history and paleoclimate. *Journal of Geophysical Research: Planets*, *125*, e2019JE006196. https://doi.org/10.1029/2019JE006196

Received 3 SEP 2019
Accepted 19 FEB 2020
Accepted article online 3 MAR 2020

Paleolakes in the Northwest Hellas Region, Mars: Implications for the Regional Geologic History and Paleoclimate

Jiannan Zhao[1,2,3], Long Xiao[1,2], and Timothy D. Glotch[4]

[1]State Key Laboratory of Geological Processes and Mineral Resources, Planetary Science Institute, School of Earth Sciences, China University of Geosciences, Wuhan, China, [2]State Key Laboratory of Lunar and Planetary Science, Macau University of Science and Technology, Macau, China, [3]School of Environmental Studies, China University of Geosciences, Wuhan, China, [4]Department of Geosciences, Stony Brook University, Stony Brook, NY, USA

Abstract Hellas basin is one of the largest and oldest impact basins on the Martian surface. Its surrounding highland regions have undergone complicated geologic processes after the formation of Hellas basin. However, the geologic and climatic histories of the highlands surrounding Hellas are still unclear. Paleolakes provide us clues to answer these questions. In this study, we made a detailed investigation of paleolakes in the northwest Hellas region with high-resolution imaging, topographic, and spectral data. A total of 64 paleolakes were identified with diameters larger than 4 km, in which 49 are newly reported. We calculated basic hydrologic parameters of the paleolakes and analyzed the sedimentary landforms, resurfacing processes, and aqueous minerals in the lake basins. Comprehensive analyses of the geomorphology, mineralogy, and age of the paleolakes revealed the geologic and climatic histories of the northwest Hellas region: a climate transition from warm and wet to semi-arid happened in Noachian, and then lakes drained in a cold and dry climate in the early Hesperian, contemporary with or followed by a period of intense volcanic activity peaked around 3.3 Ga, and finally in the Amazonian, an extensive glacial event around 0.9 Ga resurfaced most of the paleolakes in the region south of 25°S. Our study also supports the existence of a "Hellas Ocean" and indicates that the Martian climate could have variations on regional scales and further studies are still needed to clarify the details.

Plain Language Summary Paleolake basins are widely distributed on the Martian surface and have attracted high attention as they record information on regional geologic history and climate change. Hellas basin is one of the largest and oldest impact basins on the Martian surface, and it has undergone complicated geologic processes associated with climate changes. In this paper, we studied the highland region around the northwest part of the Hellas basin. Detailed study of the paleolakes in this region could provide clues to reveal the geologic and climatic history. We identified 64 paleolakes with high-resolution image and topographic data and analyzed their morphology, landforms, ages, and aqueous minerals. We found that the lakes drained around 3.6 billion years ago, contemporary with or followed by extensive volcanic activity peaked at ~3.3 billion years ago. Then, glacial activity happened in this area around 0.9 billion years ago. In addition, the distribution, morphology, and mineral composition of the paleolakes also indicate that the climate of the northwest Hellas region in Noachian may have undergone a transition from warm and wet to semi-arid.

1. Introduction

Liquid water has played a significant role in shaping the Martian surface and a variety of landforms that could be related to fluvial activity are present on Mars (Baker, 2006; McSween, 2006), for example, valley networks (Alemanno et al., 2018; Carr, 1995; Fassett & Head, 2008a; Gulick & Baker, 1989), outflow channels (Baker, 1978; Rodriguez et al., 2015), paleolakes (De Hon, 1992; Fassett & Head, 2008b; Goudge, Head, et al., 2012; Goudge, Aureli, et al., 2015), and deltas (Fassett & Head, 2005; Goudge et al., 2017, 2018; Kraal et al., 2008; Rivera-Hernández & Palucis, 2019). Among them, paleolakes have received much attention. More than 400 paleolakes have been identified in previous studies, and they are widely distributed throughout the Martian southern highlands (Cabrol & Grin, 1999, 2002; De Hon, 1992; Fassett & Head, 2008b; Goudge, Head, et al., 2012, Goudge, Aureli, et al., 2015; Newsom et al., 1996). Paleolakes are windows to

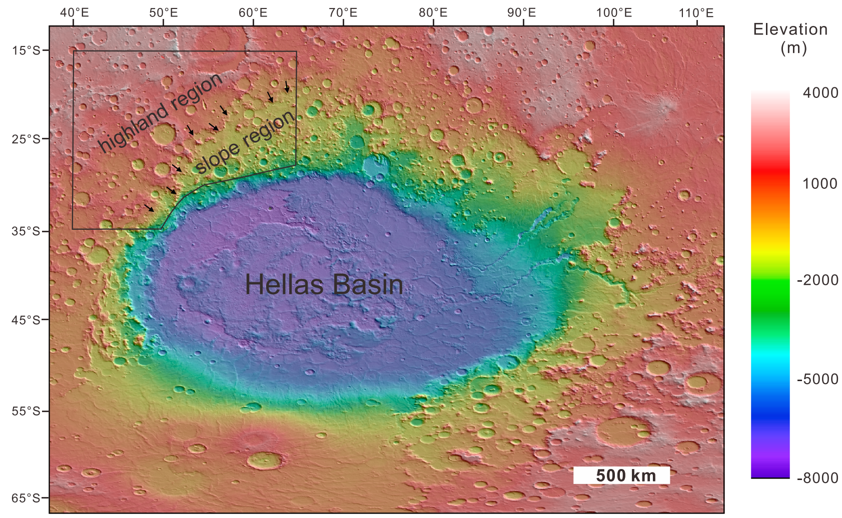

Figure 1. MOLA colorized topographic map of the Hellas region overlain on MOLA shaded relief. The area in the black polygon is our study region. The black arrows point to a discontinuous scarp between the "highland region" and "slope region" in the study area.

the regional geologic history and climatic evolution of ancient Mars (Cabrol & Grin, 2001; Eigenbrode et al., 2018; Forsythe & Blackwelder, 1998; Fukushi et al., 2019; Goldspiel & Squyres, 1991; Grotzinger et al., 2015; Irwin et al., 2005; Michalski et al., 2019): Their morphology and distribution can reflect the distribution of water, the compositions of lake deposits are indicators of hydrologic and climatic conditions, and resurfacing landforms in the lake basins can record later geologic processes and climate changes. Therefore, paleolakes have long been suggested as candidate landing sites for Martian in situ exploration missions (Grant et al., 2018; Grin & Cabrol, 1997; Haskin et al., 2005; Wray, 2012).

Previous studies mostly focused on the global identification and distribution of paleolakes (Cabrol & Grin, 1999, 2001; De Hon, 1992; Fassett & Head, 2008b; Goudge, Head, et al., 2012; Goudge, Aureli, et al., 2015) or detailed analyses of a single paleolake (Cabrol et al., 1999; Dehouck et al., 2010; Glotch & Christensen, 2005; Goudge, Mustard, et al., 2015; Grin & Cabrol, 1997; Irwin et al., 2002; Irwin et al., 2015; Michalski et al., 2019; Palucis et al., 2016; Pajola et al., 2016; Salvatore et al., 2018); nevertheless, identification and comprehensive analyses of paleolakes at regional scales are also of great significance for understanding the geologic and climatic history of an area. In this study, we chose the area located around the northwest margin of the Hellas basin as our study region (40°–65°E, 15°–35°S; Figure 1). This area has been considered as the outer part of the Hellas concentric system (Wichman & Schultz, 1989) that formed before 4.0 Ga (Bottke & Andrews-Hanna, 2017; Frey, 2008). Hellas is the largest impact basin in the Martian southern highlands, with an east-west extent of about 2,200 km and a north-south extent of 1,600 km. The study area can be divided into a "highland region" in the northwest and a "slope region" that dips toward the Hellas basin in the southeast (Figure 1) by a discontinuous scarp that has been identified as extending between 600 and −700 m around the Hellas basin (Wilson et al., 2007). The elevation decreases from ~3,500 m in the "highland region" to about −2,500 m near the margin of the Hellas basin. Geologic units of the region including a Noachian basement rock unit, a Noachian heavily cratered unit, and Noachian to Hesperian volcanic and sedimentary units have been identified in the geologic map produced by Leonard and Tanaka (2001), indicating the region's complex geologic history. Salese et al. (2016) studied the intercrater plains of the region and suggested that they have a sedimentary origin. Irwin et al. (2018) investigated the geologic characteristics of the wind-eroded crater floors and intercrater plains in the northwest of our study region and proposed a sequence of events and modification processes. Cawley and Irwin (2018) analyzed the landscape evolution of the Noachis Terra, describing the role of impact cratering, fluvial, and aeolian processes in the evolution of geomorphic features including escarpments, pediments, and plains. Cowart et al. (2019) also found widespread evidence for clastic materials in the intercrater plains of the southern highlands. However, intra-crater materials are rarely studied although several craters have been identified as paleolake basins

(Goudge, Head, et al., 2012, Goudge, Aureli, et al., 2015), which lead to an incomprehensive understanding of the regional geologic and climatic record. Besides, as a representative of transition zones from the highlands regions to deep catchment basins, it is important to depict the geologic and climate change of this region. Therefore, we made a detailed survey of the paleolakes in the northwest Hellas region with high-resolution image and topographic data to analyze the sedimentary landforms, resurfacing processes, and ages of different geologic events to constrain the geologic history of the northwest Hellas region. We also investigated the types and distribution of aqueous minerals in the paleolakes, utilizing newly acquired spectral data, together with the analyses of paleolake morphology, to shed light on the paleoclimate of the region.

2. Data and Methods

2.1. Identification and Geomorphologic Analyses of Paleolake Basins

Paleolakes are usually formed in topographic lows. As craters are widely distributed in Martian southern highlands and they usually occupy local lows, crater-hosted paleolakes are most common (Cabrol & Grin, 1999; Goudge, Aureli, et al., 2015). They are composed of a crater basin and valleys breaching the crater rim. Paleolakes have been divided into two types based on their hydrology, that is, open-basin lakes and closed-basin lakes (Cabrol & Grin, 1999; Goudge, Head, et al., 2012). Typical open-basin lakes have both inlet and outlet valleys. The inlet valley shows a longitudinal elevation decrease to the crater basin, while the outlet valley has an elevation decrease away from the basin. Crater basins that only have outlet valleys but no obvious inlet valleys have also been regarded as open-basin lakes (Warner et al., 2010). Closed-basin lakes have at least one inlet valley that breaches the crater rim but have no outlet valleys. It should be noted that some other geologic processes may produce similar landforms as paleolakes. For example, some candidate paleolakes could be formed by volcanic activity (Leverington, 2006; Leverington & Maxwell, 2004). Therefore, in this study, we also considered morphologic features (e.g., sedimentary landforms and inlet types) and mineralogy of the candidate paleolakes to provide a confidence level, and three categories have been proposed. Basins that satisfy both the following two constraints were classified as “Confident”: (1) connected with networks of inlet valleys or single valleys and (2) have sedimentary landforms (e.g., deltas and layered deposits) or aqueous minerals. Basins connected with networks of inlet valleys without mineralogical evidence nor typical sedimentary landforms belong to “Probable” as branching upstream valleys are commonly formed by fluvial processes rather than lava flows. The rest of the candidate paleolakes that have single inlet valleys were classified as “Possible.”

Based on these criteria, we used the 100-m-per-pixel daytime IR mosaics from the Mars Odyssey Thermal Emission Imaging System (THEMIS) as a regional context image and 6-m-per-pixel Mars Reconnaissance Orbiter Context Camera (CTX) images and 200-m-per-pixel digital elevation models (DEMs) produced from blended High Resolution Stereo Camera and Mars Orbiter Laser Altimeter data to identify paleolakes and analyze their morphology. In addition, high-resolution DEMs produced by CTX stereopairs with the Ames Stereo Pipeline (Shean et al., 2011) were also used to help identify and study the paleolakes. HiRISE (High Resolution Imaging Science Experiment) images, which have a resolution of ~0.25 m per pixel, were used to make detailed analyses of the geomorphologic features.

We also measured the hydrologic parameters of the paleolakes with High Resolution Stereo Camera/Mars Orbiter Laser Altimeter-blended DEM and CTX images. The maximum lake surface elevation (Max. Elev.) of an open-basin lake is determined based on the elevation of the site where the outlet valley breaches the basin rim. For a closed-basin lake, Max. Elev. is defined as the elevation of the lowest point on the crest of a basin rim (Goudge, Aureli, et al., 2015). Then, the lake area, lake volume, and mean depth could be calculated according to the method proposed by Fassett and Head (2008b) using the DEM data. We also measured the length of the longest inlet valley for each paleolake (Inlet Length). This parameter could be an indicator of the water sources of lakes and is used to divide the closed-basin lakes into two types: lakes with short inlet valleys (less than 20 km; Type C_1) and those with long inlet valleys (at least one inlet valley longer than 20 km; Type C_2) (Goudge, Aureli, et al., 2015).

2.2. Age Determination

We performed crater size-frequency distribution measurements (Michael & Neukum, 2010) on different geologic units to acquire ages of the paleolakes and time of the resurfacing events. Irregular craters, crater chains, and clusters were eliminated in crater counting to minimize the influence of secondary craters.

The absolute model ages were based on the production function and chronology curve proposed by Neukum et al. (2001) and Hartmann and Neukum (2001), respectively. As resurfacing events occurred extensively in the paleolake basins, older units are likely partially resurfaced, resulting in a "kink" in the size-frequency distribution plots. In this situation, a resurfacing correction was carried out according to the method suggested by Michael and Neukum (2010) to obtain the ages for each portion of the distribution: The older age represents the age of the original surface, while the younger age corresponds to the age of the resurfacing event. The results of age determination were then used in the reconstruction of geologic history of the study area. It should be noted that some paleolake basins occupied relatively small area or were highly modified, making it hard to constrain their ages or leading to large dating error ranges, which could affect the certainty of the geologic history.

2.3. Identification of Aqueous Minerals

CRISM (Compact Reconnaissance Imaging Spectrometer for Mars) and THEMIS spectral data were used to identify aqueous minerals and anhydrous chloride salts. We checked all the CRISM targeted observation data overlapping the paleolake basins in the northwest Hellas region to search for phyllosilicates and evaporites. CRISM data cover the spectral range of 0.36–3.92 μm and have spatial resolution of 18 m per pixel (full resolution targeted [FRT] and full resolution short [FRS]) or 36 m per pixel (half resolution long [HRL] and half resolution short [HRS]), which is suitable for the identification of many aqueous minerals such as sulfates, carbonates, and phyllosilicates (Murchie et al., 2007; Pelkey et al., 2007; Viviano-Beck et al., 2014). Atmospheric correction and spectral analyses were performed utilizing the CRISM Analysis Toolkit (Version 7.3.1) based on the methods proposed by McGuire et al. (2009) and Viviano-Beck et al. (2014).

However, as chlorides are difficult to identify with visible and near-infrared data due to lack of diagnostic absorptions, we produced THEMIS surface emissivity data and THEMIS decorrelation stretched (DCS) composites based on the methods proposed by Bandfield (2004) to identify the presence of chlorides. THEMIS covers the 6.7- to 14.8-μm spectral region with nine narrow band channels (Christensen et al., 2004). Chlorides exhibit a blue slope in THEMIS spectra and appear blue and green in DCS 8-7-5 and 9-6-4 composites, respectively (Glotch et al., 2010, 2016; Osterloo et al., 2008; Osterloo et al., 2010).

3. Results

3.1. Distribution and Morphology of the Paleolakes

A total of 64 paleolake basins with diameters larger than 4 km were identified in our study region, including 15 open-basin lakes and 49 closed-basin lakes (Figure 2 and Table 1). Among them, 12 open-basin lakes and 37 closed-basin lakes were newly recognized. The estimation of confidence levels shows that the number of paleolakes with "Confident," "Probable," and "Possible," levels is 33, 19, and 12, respectively. Based on the inlet length, 40 closed-basin lakes belong to Type C_1, while the other nine closed-basin lakes were classified as Type C_2. The inlet lengths of the lakes range from several kilometers to nearly 100 km, and most of them are less than 30 km (Table 1 and Figure 3a). Most of the lake basins are circular in shape, and their host craters have diameters from 4.6 to 75.3 km. The estimated lake areas vary from 4.0 to ~1.9×10^4 km^2, and the estimated lake volumes range from 0.06 to ~2.9×10^4 km^3 (Table 1 and Figures 3c and 3d). It should be noted that lake volumes are calculated based on the present basin topography; thus, there could be an underestimate as basins may have been filled with other materials (e.g., lava, volcanic ash, and crater ejecta) after drying up. On the other hand, as closed-basin lakes do not have outlet valleys, it is debatable whether water had accumulated to the estimated lake area and volume. We also calculated the mean depth of the lakes according to the lake volume and area, obtaining results ranging from 8 to 1,490 m (Table 1).

The distribution of the paleolakes shows that more than half (~53%) of the open-basin lakes are located near (<20 km) the discontinuous scarp northwest of Hellas (Figure 2). In contrast, closed-basin lakes can be found all over the area. Analyses of maximum lake surface elevations show that the paleolakes are distributed from near 2,000 to near 3,000 m in elevation (Table 1), and there is a high concentration of closed-basin lakes in the range of 1,000–2,000 m (Figure 3b). In addition, the density of paleolakes in the "highland region" is ~50 per million square kilometers, which is about 25% higher than that in the "slope region" (~40 per million square kilometers) (Figure 2).

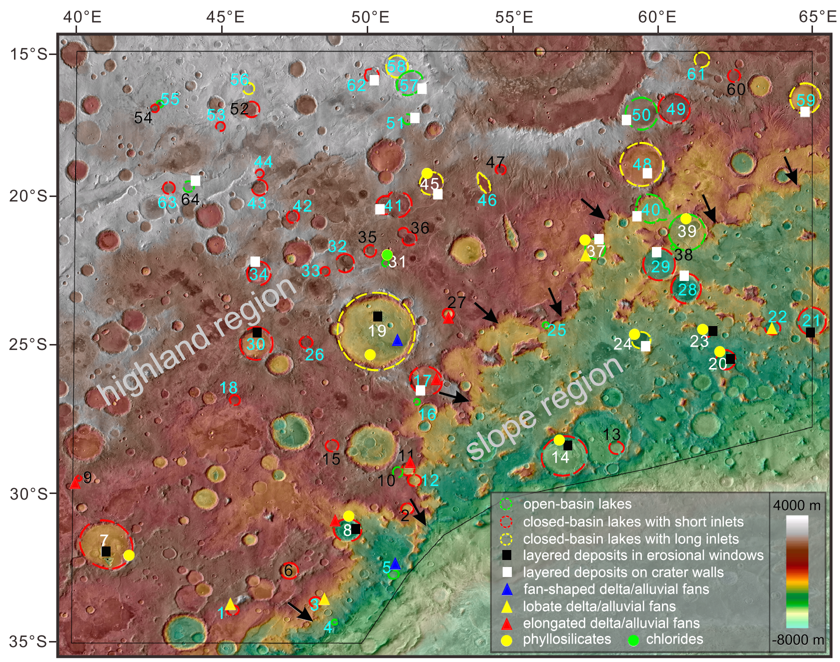

Figure 2. Distribution of paleolakes (dashed circles) in northwest Hellas. Colors of the paleolake numbering indicate different confidence levels of the paleolakes (cyan, "Confident"; white, "Probable"; black, "Possible"). Red and yellow circles denote closed-basin lakes with short (Type C_1) and long (Type C_2) inlet valleys, respectively. Green circles denote open-basin lakes. The locations of sedimentary landforms and aqueous minerals identified in the lake basins were also marked by different symbols as indicated in the inset of the figure. Black arrows indicate the location of discontinuous scarps. The background is THEMIS daytime IR mosaic overlain by colorized HRSC/MOLA-blended DEM.

3.2. Sedimentary Landforms in the Paleolakes

Although the paleolakes in the study region have undergone diverse modification processes, sedimentary materials can still be observed in some of the lake basins. These materials are usually light- to intermediate-toned and look relatively smooth in high-resolution images. Sedimentary landforms in the paleolakes are mainly deltas/alluvial fans and layered deposits. A total of 11 (~17.2%) paleolakes contain deltas/alluvial fans, and 24 paleolakes have layered deposits, accounting for 37.5% of the total (Table 1 and Figure 4).

3.2.1. Deltas/Alluvial Fans

Fan-shaped landforms are common on the Martian surface, and they could be formed in various geologic processes such as fluvial (Cabrol & Grin, 2001; Rivera-Hernández & Palucis, 2019), glacial (Pathare et al., 2017), volcanic (Noe Dobrea et al., 2006; Skilling, 2002), and mass wasting (Irwin et al., 2014). These processes lead to differences in detailed morphologic characteristics. For example, fan-shaped glacial deposits are usually related to glacial tills or viscous flow features (Li et al., 2005; Milliken et al., 2003); lava deltas are commonly fed by lava tubes and exhibit a collapsed delta toe (Goudge, Mustard, et al., 2012; Skilling, 2002); fans formed by mass wasting are prone to retreated backwalls or theater-shaped collapse. After eliminating the fans unrelated to fluvial processes, we identified 11 deltas/alluvial fans in the paleolakes (supporting information Figure S1). Most of them are relatively small with the largest one covering an area of ~35 km^2. They could be roughly divided into three types based on the scheme proposed by Cabrol and Grin (2001): fan-like, elongated, and lobate (Figures 4a and 5). A fan-like delta has a typical length/width ratio of 1 and can vary between 0.7 and 1.8; an elongated delta has a length/width ratio of larger than 1.8 (typically 2.7); a lobate delta is less than 0.7 in the length/width ratio (typically 0.4) (Cabrol & Grin, 2001). Fan-like delta/alluvial fans (Figure 5a) were found in paleolakes No. 5 and 19, and both of them are less than 1 km^2. Elongated delta/alluvial fans (Figure 5b) are present in 5 paleolakes and the longest one extends about 5 km. Four lobate delta/alluvial fans were identified. Among them, the lobate delta in paleolake No. 37 (Figure 5c) is the largest delta/alluvial fan in the study region. It is located at the mouth of the

Table 1
Basic Parameters of the Paleolakes in the Study Region

Paleolake No.	Lon. (°E)	Lat. (°S)	Type	Inlet length (km)	Inlet type	Max. Elev. (m)	Lake area (km^2)	Lake volume (km^3)	Mean depth (m)	R_{crater} (km)	Type of deltas/fans	Type of layering	Type of aqueous mineral	Dominant resurfacing process	Confidence level
1*	45.31	33.88	C_1	8.4	VN	878	278.9	63.0	226	9.9	Lobate	/	/	G	Confident
2	51.26	30.43	C_1	4.8	SV	525	305.0	108.9	357	11.0	/	/	/	G	Possible
3*	48.11	33.61	C_1	6.2	VN	−96	232.5	35.0	151	10.3	Lobate	/	/	G	Confident
4	48.76	34.29	O	22.2	VN	−1,091	25.8	1.0	39	5.8	/	/	/	G	Probable
5	50.77	32.67	O	13.9	VN	−2,070	62.0	1.7	27	8.6	Fan-like	/	/	G	Confident
6	47.23	32.55	C_1	7.1	SV	819	886.8	405.9	458	17.2	/	/	/	G	Possible
7	40.94	31.69	C_1	17.7	VN	820	7,669.4	4,188.3	546	50.1	/	EW	Smectite	G	Confident
8	49.19	31.17	C_1	8.2	VN	−321	1,906.8	1,752.3	919	24.3	Elongated	EW	Smectite	G	Confident
9	40.07	29.42	C_1	9.1	SV	1,193	90.4	7.9	87	5.8	Elongated	/	/	U	Confident
10	50.89	29.19	O	3.2	SV	982	93.1	1.4	15	10.8	/	/	/	G	Possible
11	51.25	29.11	C_1	7.5	SV	134	267.2	49.4	185	13.1	Elongated	/	/	G	Confident
12	51.47	29.49	C_1	6.2	VN	18	197.6	21.5	109	12.1	/	/	/	G	Probable
13	58.36	28.35	C_1	7.8	SV	−2,030	555.7	424.9	765	13.6	/	/	/	U	Possible
14	56.53	28.60	C_1	15.4	VN	−1,544	5,416.7	4,803.1	887	45.0	/	EW	Smectite	G	Confident
15	48.69	28.31	C_1	3.4	SV	1,027	414.0	109.4	264	11.3	/	/	/	U	Possible
16	51.56	26.82	O	14.3	VN	632	7.2	0.06	8	6.2	/	/	/	U	Probable
17	51.89	26.09	C_1	18.4	VN	700	1,939.8	245.8	127	30.3	Elongated	CW	/	V	Confident
18	45.37	26.76	C_1	15.2	VN	791	116.3	4.2	36	10.9	/	/	/	U	Probable
19	50.20	24.41	C_2	34.1	VN	1,500	1,9255.8	28,699.8	1,490	75.3	Fan-like	EW	Smectite	V	Confident
20	62.06	25.39	C_1	3.7	SV	−1,269	1,100.8	410.7	373	19.5	/	EW	Smectite	V	Confident
21	64.99	24.11	C_1	12.2	VN	−535	2,219.7	823.6	371	29.1	/	EW	/	V	Confident
22	63.67	24.33	C_1	9.5	VN	−853	588.3	307.5	522.7	14.0	Lobate	/	/	U	Confident
23	61.40	24.51	C_1	6.2	SV	−1,027	14.8	0.7	47	9.1	/	EW	Smectite	U	Confident
24	59.18	24.74	C_2	28.3	VN	−867	885.4	116.5	132	18.1	/	CW	Smectite	V	Confident
25	55.95	24.23	O	9.6	VN	24	72.9	23.2	318	5.9	/	/	/	U	Probable
26	47.80	24.80	C_1	16.8	VN	1,210	402.8	18.5	46	11.9	/	/	/	U	Probable
27*	52.63	23.84	C_1	4.9	SV	1,116	353.2	253.6	718	11.2	Elongated	/	/	U	Confident
28	60.69	22.98	C_1	14.2	VN	−474	2,510.5	1,501.5	598	29.4	/	CW	/	V	Confident
29	59.79	22.16	C_1	9.1	VN	−512	3,232.8	1,601.9	496	32.6	/	CW	/	V	Confident
30	46.11	24.87	C_1	13.8	VN	1,533	3,362.4	3,150.3	937	32.3	/	EW	/	U	Confident
31	50.49	22.11	O	19.2	VN	1,640	4.0	0.08	20	7.5	/	/	Chloride	U	Confident
32	49.13	22.13	C_1	12.6	VN	1,792	964.1	160.6	166	17.2	/	/	/	U	Probable
33	48.44	22.41	C_1	6.7	VN	1,699	209.1	26.3	126	9.1	/	/	/	U	Probable
34	46.19	22.47	C_1	11.1	VN	1,715	1,589.4	1,117.8	703	23.5	/	CW	/	U	Confident
35	49.96	21.71	C_1	13.1	SV	1,676	487.7	82.2	168.5	12.2	/	/	/	U	Possible
36	51.24	21.21	C_1	4.6	SV	1,157	746.0	83.6	112	/	/	/	/	U	Possible
37*	57.61	21.64	O	95.1	VN	−85	134.1	6.1	45	19.7	Lobate	CW	Smectite	U	Confident
38	60.28	21.58	O	/	/	−123	8.6	0.6	70	4.6	/	/	/	U	Possible
39*	60.79	21.04	O	18.4	VN	−287	1,138.4	123.8	109	36.2	/	/	Smectite	V	Confident
40*	59.50	20.26	O	23.2	VN	−205	1,395.1	163.3	117	/	/	CW	/	U	Confident
41	50.78	20.11	C_1	15.1	VN	1,407	2,298.8	548.9	239	/	/	CW	/	V	Confident
42*	47.37	20.54	C_1	8.5	VN	1,165	368.9	93.5	253	11.8	/	/	/	U	Probable
43*	46.21	19.58	C_1	7.3	VN	1,944	630.6	326.4	518	15.3	/	/	/	U	Probable
44	46.22	19.09	C_1	14.5	VN	2,289	25.8	0.4	16	7.7	/	/	/	U	Probable
45*	52.06	19.42	C_2	27.6	VN	1,359	1,697.0	334.3	197	23.9	/	CW	Smectite	V	Confident
46*	53.87	19.43	C_2	76.1	VN	1,295	629.5	236.4	376	/	/	/	/	U	Probable
47	54.42	18.97	C_1	7.5	SV	1,621	332.8	179.1	538	10.9	/	/	/	U	Possible

10.1029/2019JE006196

Table 1 *(continued)*

Paleolake No.	Lon. (°E)	Lat. (°S)	Type	Inlet length (km)	Inlet type	Max. Elev. (m)	Lake area (km^2)	Lake volume (km^3)	Mean depth (m)	R_{crater} (km)	Type of deltas/fans	Type of layering	Type of aqueous mineral	Dominant resurfacing process	Confidence level
48*	59.18	18.80	C_2	87.2	VN	992	5,782.0	2,904.6	502	46.3	/	CW	/	V	Confident
49	60.32	16.87	C_1	18.9	VN	1,219	1,933.2	318.0	164	31.3	/	/	/	V	Probable
50	59.16	17.02	O	22.3	VN	1,742	1,294.2	176.4	136	32.8	/	CW	/	V	Confident
51	51.25	17.24	O	8.3	SV	2,074	102.9	11.0	107	10.2	/	CW	/	U	Confident
52*	45.92	16.91	C_1	5.4	SV	1,814	633.3	321.7	508	16.6	/	/	/	V	Possible
53*	44.87	17.49	C_1	13.6	VN	2,305	153.2	16.0	104	9.0	/	/	/	U	Probable
54	42.66	16.88	C_1	2.7	SV	2,202	158.0	36.0	228	7.9	/	/	/	U	Possible
55	42.83	16.72	O	7.3	VN	2,120	9.3	0.3	32	6.5	/	/	/	U	Probable
56*	45.84	16.21	C_2	28.8	VN	2,627	354.0	65.0	184	11.3	/	/	/	U	Probable
57	51.33	15.99	O	27.4	VN	2,626	1,271.4	126.1	99	27.2	/	CW	/	V	Confident
58	50.85	15.46	C_2	34.0	VN	2,613	1,179.4	81.8	69	23.2	/	/	/	U	Probable
59	64.76	16.54	C_2	23.9	VN	870	2,592.4	1,635.6	631	30.7	/	CW	/	V	Confident
60	62.23	15.77	C_1	3.9	SV	1,457	478.2	126.5	265	12.8	/	/	/	V	Possible
61*	61.25	15.24	C_2	31.4	VN	1,410	459.8	70.2	153	16.0	/	/	/	V	Probable
62	50.04	15.68	C_1	4.9	VN	2,324	487.6	51.8	106	/	/	CW	/	U	Confident
63	43.12	19.57	C_1	11.3	VN	2,074	379.5	48.2	127	11.7	/	/	/	U	Probable
64	43.82	19.54	O	6.5	SV	2,323	249.1	32.7	131	10.4	/	CW	/	U	Confident

Note. "/" means unavailable.
Abbreviations: Lon. = longitude; Lat. = latitude; Max. Elev. = maximum lake surface elevation; R_{crater} = radius of the host crater; C_1 = Type C_1 closed-basin lake; C_2 = Type C_2 closed-basin lake; O = open-basin lake; SV = single valley; VN = valley network; EW = erosional window; CW = crater wall; G = glacial; V = volcanic; U = undetermined.
*Denotes the paleolakes already identified by Goudge, Head, et al. (2012) and Goudge, Aureli, et al. (2015).

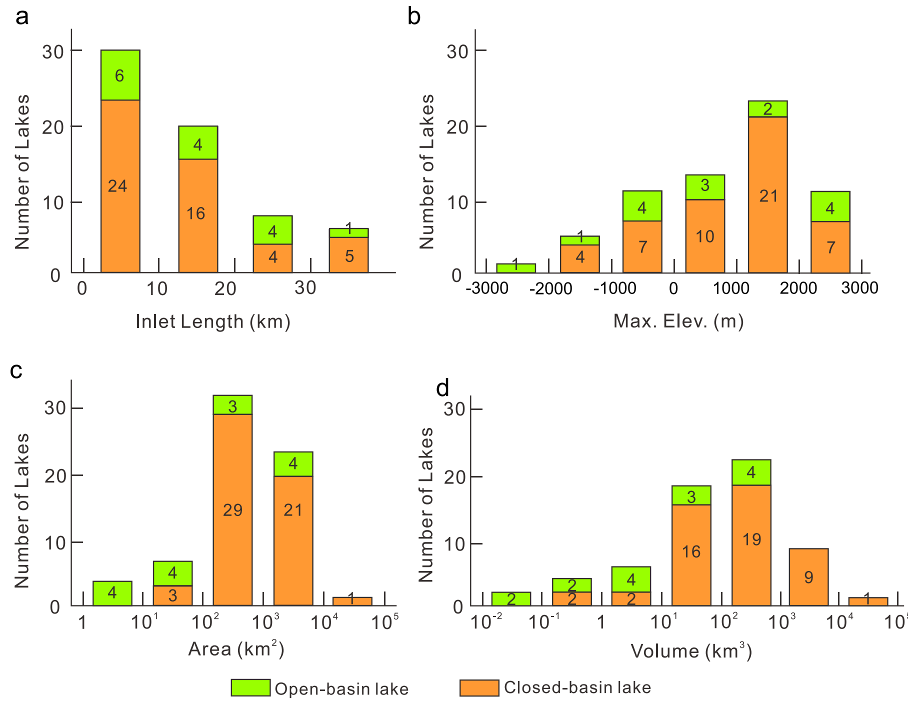

Figure 3. Distribution of (a) inlet lengths, (b) maximum lake surface elevation (Max. Elev.), (c) lake area, and (d) lake volume for the identified lakes.

inlet valley and extends about 12 km in the north-south direction and 4 km in the east-west direction. Several small near-parallel channels are present on the delta and they extend outside the delta to the east and southeast. Materials transported by the small valleys filled the depressions (pointed by yellow arrows in Figure 5c) in the basin floor, which may indicate a later stage of fluvial activity.

3.2.2. Layered Deposits

Layered deposits are widely distributed in our study region and they may have origins other than lacustrine deposits, such as volcanic ashes, aeolian sand deposits, exposure of bedrocks, and impact breccia/melts. Volcanic ashes usually spread in a large area regardless of intercrater plains or crater basins (Ansan et al., 2011). Aeolian deposits show very-fine grain and rarely have continuous near-horizontal beddings (Ansan et al., 2011; Salese et al., 2016). Exposure of layered bedrocks are commonly seen in intercrater plains or the wall of basins rather than crater floors (e.g., Squyres et al., 2006). Impact breccia or melts commonly form layers draping preexisting topography instead of settling into an equipotential surface (Mustard et al., 2007). Based on the abovementioned features, we excluded layered deposits of other origins and followed the

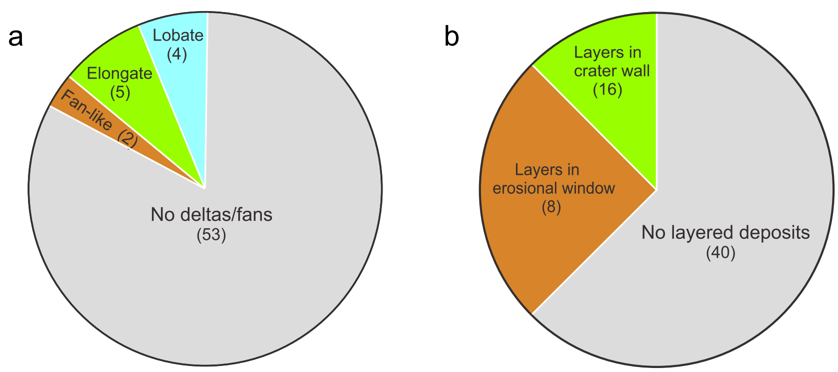

Figure 4. Numbers of different types of (a) deltas/alluvial fans and (b) layered deposits.

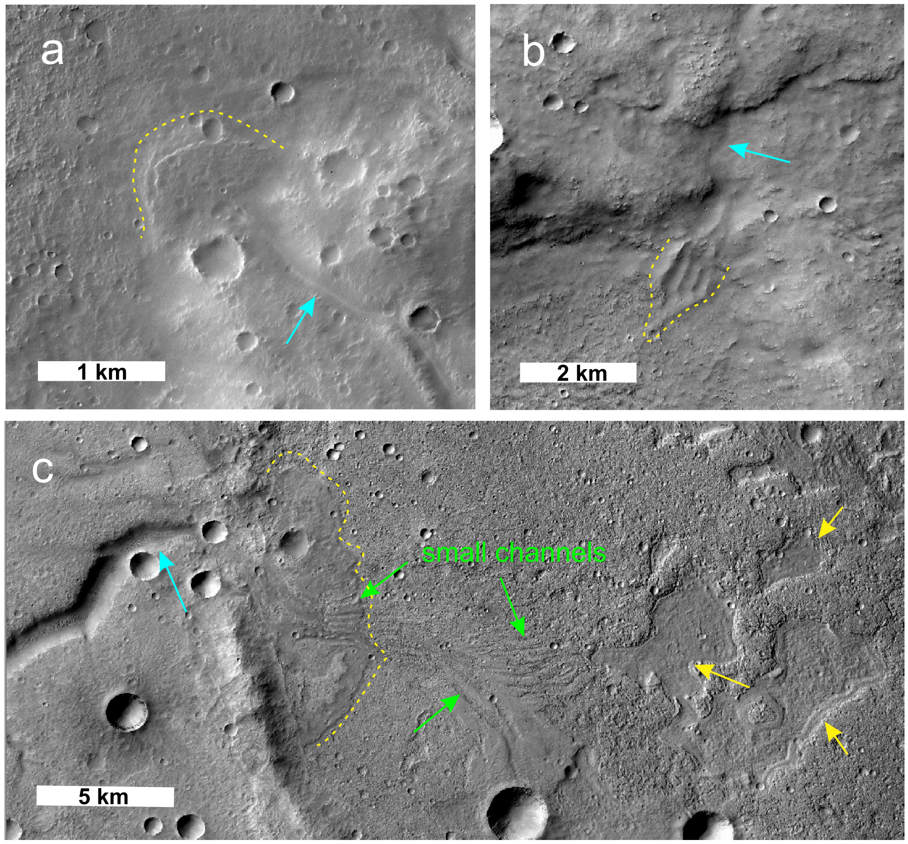

Figure 5. Different types of deltas/alluvial fans found in the study region. Cyan arrows point to the inlet valleys, and dashed lines indicated the margins of the deltas/alluvial fans. (a) A fan-like delta/alluvial fan in paleolake No. 19. CTX ID: B01_010128_1554_XI_24S309W. (b) An elongated delta/alluvial fan in paleolake No. 9. CTX ID: F17_042633 _1511_XI_28S320W. (c) A lobate delta in paleolake No. 37. Green arrows indicate the small channels. Yellow arrows point to the filled depressions. CTX ID: D16_033652_1581_XN_21S302W, B03_010642_1561_XI_23S302W.

criteria proposed by Goudge, Head, et al. (2012) to identify lacustrine layered deposits. A total of 24 sites were identified (Table 1) and they usually occurred in erosional windows (Figure 6a) or on the walls of craters (Figure 6b) in the paleolake basins. As the former usually have well-exposed profiles, we focused on the layered deposits in the erosional windows identified in eight lake basins. The thicknesses of these exposed layered deposits ranges from around 100 m to more than 1 km. A typical erosional window with thick layered deposits in paleolake No. 7 is shown in Figure 7. The erosional window which has a triangular shape

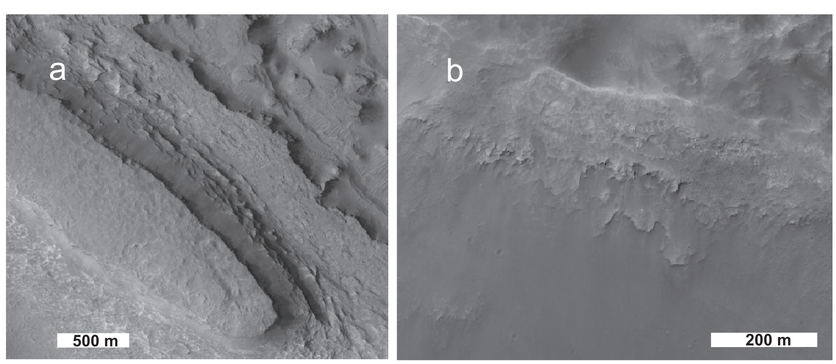

Figure 6. (a) Layered deposits in an erosional window of paleolake No. 14. HiRISE ID: ESP_020835_1510_RED. (b) Layered deposits on the wall of a crater in paleolake No. 29. HiRISE ID: ESP_023393_1575_RED.

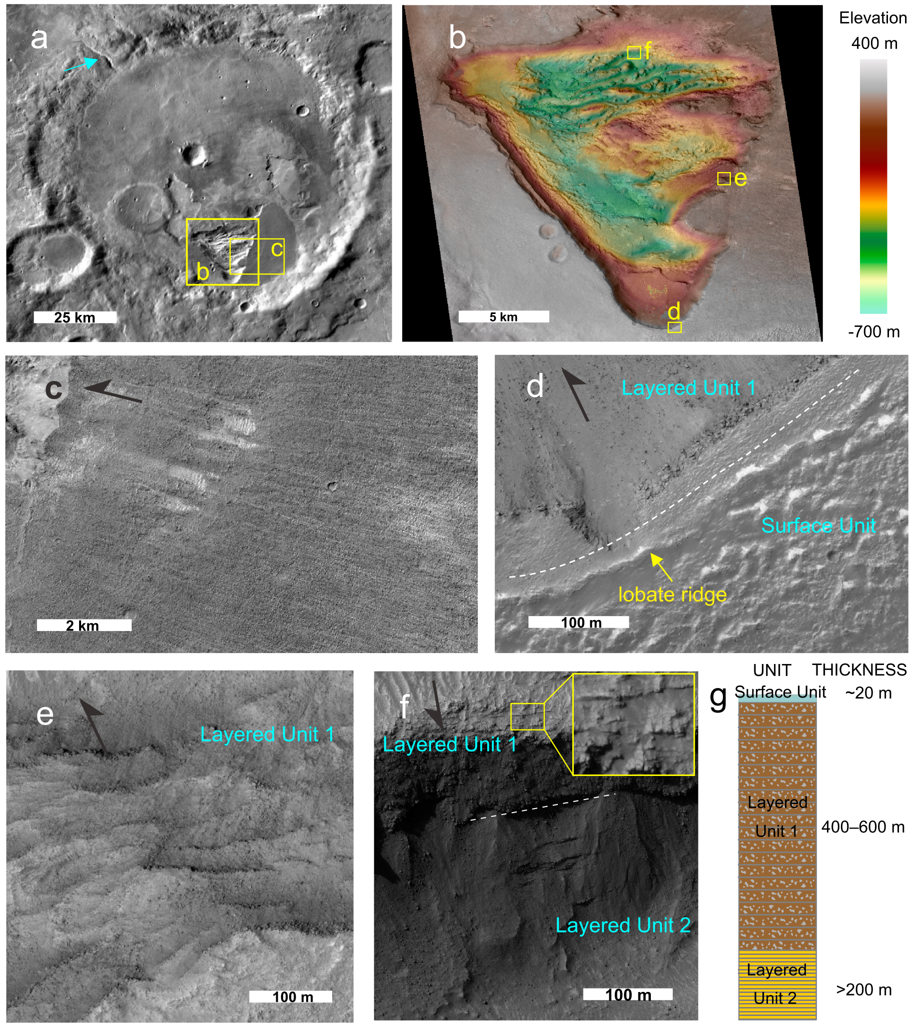

Figure 7. Layered deposits in an erosional window of paleolake No. 7. (a) THEMIS Daytime IR mosaics of the paleolake No. 7. The erosional window (central coordinates are 40.94°E, 31.69°S) is located in the southern part of the basin floor. Yellow boxes indicate the location of other pictures. (b) CTX image overlain by CTX DEM. Yellow boxes indicate the location of other pictures. CTX image ID: P15_006885_1473_XN_32S318W. The CTX DEM is produced from CTX stereo images ID: P15_006885_1473_XN_32S318W and F09_039376_1477_XN_32S319W. (c) Lineated terrain in the Surface Unit. The black arrow points to downslope. CTX image: P15_006885_1473_XN_32S318W. (d) HiRISE image of the boundary of the Surface Unit and Layered Unit 1 (indicated by white dashed line). A lobate ridge (pointed by the yellow arrow) extends along the boundary. The black arrow points to downslope. HiRISE ID: PSP_006885_1475_RED. (e) HiRISE image of the Layered Unit 1. The black arrow points to downslope. HiRISE ID: ESP_056993_1475_RED. (f) HiRISE image of the boundary of the Layered Units 1 & 2 (indicated by white dashed line). The inset is a zoom of the fractures on the surface of an exposed layer in Layered Unit 1. HiRISE ID: PSP_006885_1475_RED. (g) A schematic figure shows the vertical thickness of different units.

covers an area of ~220 km^2 and has a maximum depth of ~900 m. From the top to the bottom, different units could be identified. The uppermost unit (Surface Unit) is characterized by ~20 m thick glacial deposits which is indicated by possible glacial landforms such as lineated terrain (Figure 7c) and a lobate ridge (Figure 7d) (Dickson et al., 2010). The next unit is Layered Unit 1, which is characterized by relatively thick subparallel layers containing coarse materials. Each layer is about 3–5 m thick and boulders up to 3 m in diameter are widely distributed in these layers (Figures 7e and 7f). The layers are relatively indurated and the surfaces of some exposed layers show a fractured pattern (inset in Figure 7f). The overall thickness of Layered Unit 1 changes from ~400 m in the north of the erosional window to ~600 m in the south. The last unit exposed in the erosional window is Layered Unit 2, which is comprised of thin (less than 1m) parallel layers. This

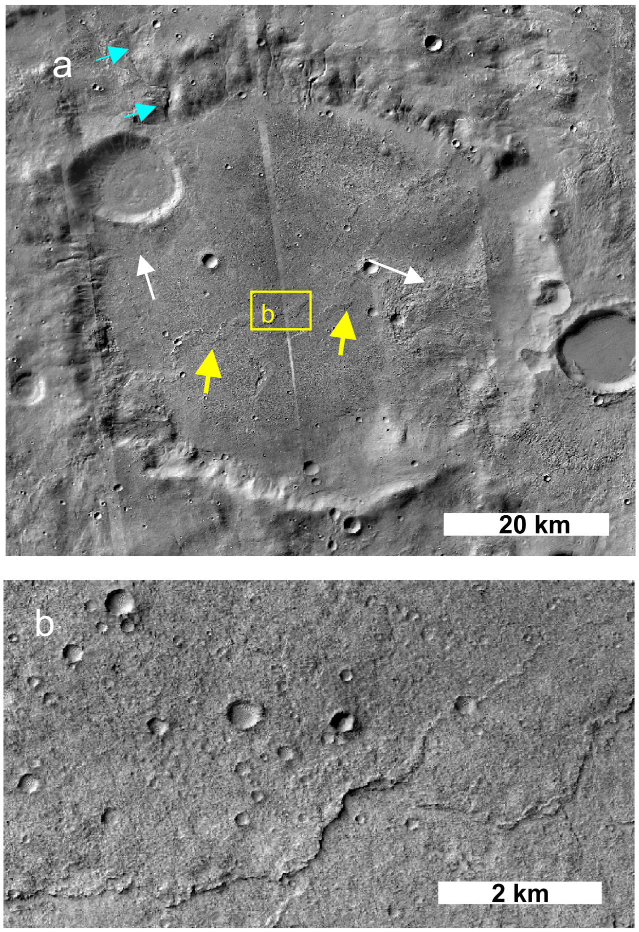

Figure 8. Volcanic resurfacing in paleolake No. 17. (a) CTX mosaics of the paleolake No. 17 (Central coordinates: 51.89°E, 26.09°S). Wrinkle ridges can be observed in the basin floor (yellow arrows). Cyan arrows indicate the inlet valley. White arrows indicate crater ejecta blankets. The yellow box shows the location of (b); (b) a zoom of the region in the box in (a) shows wrinkle ridges and the surface details. CTX ID: G17_025002_1546_XN_25S308W.

unit is composed of light-toned fine materials and the overall thickness of the Layered Unit 2 can be more than 200 m in the north of the erosional window.

3.3. Resurfacing Processes in the Lake Basins

A variety of resurfacing processes occurred in the lake basins, and they are significant in understanding the regional geologic history. Volcanic and glacial processes can dramatically resurface the original basin floors, while other geologic processes such as impact cratering and wind erosion could locally modify the paleolakes. We investigated and identified the dominant resurfacing process of each paleolake basin (Table 1).

3.3.1. Volcanic Resurfacing

Volcanic resurfacing usually exhibits the following characteristics: (1) existence of typical volcanic features such as wrinkle ridges, volcanic vents, lava flow fronts, or lobate ridges along the margin of basin floors that indicate superposition of lava flows (Goudge, Head, et al., 2012; Goudge, Mustard, et al., 2012); (2) relatively smooth in low-resolution image but looks rough in high-resolution images (e.g., CTX images in resolution higher than 8,192 pixels per degree); (3) good preservation of small craters due to relatively indurated and resistant surface materials (Fassett & Head, 2008b; Goudge, Mustard, et al., 2012; Rogers et al., 2018); and (4) show dark tones (low albedo) on visible images (Goudge, Mustard, et al., 2012). It is notable that although a moderate-to-high thermal inertia had been suggested as an indicator of volcanic surfaces by earlier studies (Goudge, Mustard, et al., 2012; Rogers & Nazarian, 2013), Rogers et al. (2018) found that many basaltic units exhibit low-to-moderate thermal inertia measured from orbit. Based on these criteria, volcanic resurfacing was observed in 18 paleolakes (Table 1). For example, paleolake No. 17 (Figure 8) shows various volcanic resurfacing characteristics. The central and northeastern parts have a dark tone in CTX mosaics, and wrinkle ridges extend across the basin floor (Figure 8a). At high resolution, a rough surface and well-preserved small craters can be observed (Figure 8b). Notably, the basin was later resurfaced by the ejecta from two large craters on the basin rim (Figure 8a). The source of the lava is difficult to identify, which could be buried by crater ejecta or due to magma transportation by feeding dikes formed along the fractures under the basin surface according to the scenario proposed by Edwards et al. (2014).

3.3.2. Glacial Resurfacing

Glacial resurfacing is characterized by a variety of landforms such as terrain softening (Squyres & Carr, 1986), ring-mold craters (Kress & Head, 2008), viscous flow features (Milliken et al., 2003), concentric crater fill (Levy et al., 2010; Squyres, 1979), and so on. Glacial resurfacing occurred in 12 paleolakes; all of which are located at higher latitude (south of ~25°S). Paleolake No. 1 (Figure 9a) is a representative of them. Its rim has a gentle slope and smooth surface that are typical characteristics of terrain softening. Ring-mold craters (Figure 9b), which could be formed by impacts into ice-rich regolith, were observed on the basin floor. Glacial-like features also occurred along the inlet valley and rocks as large as tens of meters spread along the tail of the feature and formed a terminal moraine (Figure 9c).

3.3.3. Other Resurfacing Processes

Except for volcanic and glacial activities, other geologic processes such as aeolian erosion and deposition and impact cratering could have also led to the resurfacing of paleolake basins. Impact cratering is one of the most common geologic processes on planetary surfaces. All of the paleolake basins are locally resurfaced by craters and ejecta (e.g., Figure 8a). Aeolian processes also pervasively resurfaced the surface of paleolake basin floors. The lower elevations of basin floors relative to their surroundings make paleolakes natural wind traps and may endure heavier erosion than intercrater plains. For example, paleolake No. 48 (Figure 10a)

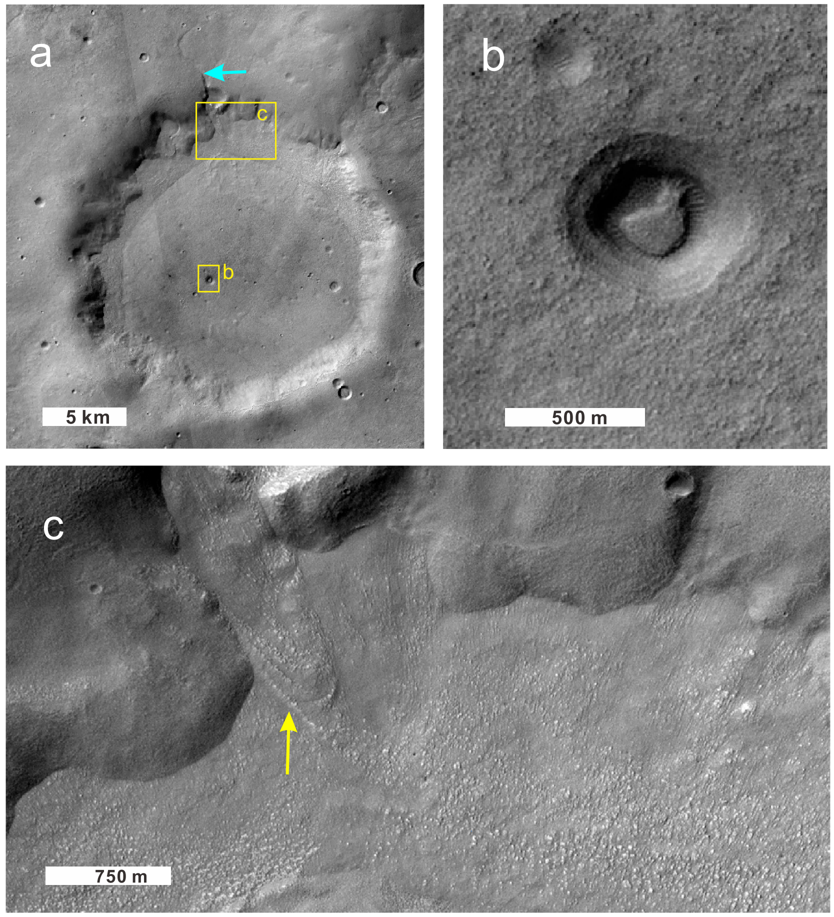

Figure 9. Glacial resurfacing in paleolake No. 1. (a) CTX mosaics of paleolake No. 1 (Central coordinates: 45.31°E, 33.88°S). Features of terrain softening are obvious. The cyan arrow points to the inlet valley. Boxes show the location of (b) and (c); (b) a ring-mold crater on the basin floor; (c) glacial-like features (indicated by the yellow arrow) near the basin rim. CTX ID: G15_023921_1452_XN_34S314W.

which is dominated by volcanic resurfacing also shows aeolian features locally such as dunes and yardangs (Figure 10b). These yardang fields can expose subsurface layers (Figure 10d) and could be the initial form of erosional windows described in section 3.2.2. In addition, a topographically inverted impact crater also indicates strong wind erosion after its floor was filled by lava (Figures 10c and 10e).

In addition to the mechanisms described above, dust mantling, deposition of volcanic ash, and sublimation of water ice or dry ice are also possible factors resulting in resurfacing (Goudge, Head, et al., 2012). These diverse processes usually make it difficult to determine the dominant resurfacing process in a paleolake and such paleolakes were labeled as “Undetermined” resurfacing process in Table 1.

3.4. Age Determination

We utilized crater size-frequency distribution measurements (Fassett, 2016; Michael & Neukum, 2010) to constrain the ages of the sedimentary units as well as the volcanic and glacial resurfacing units within the paleolake basins in order to provide a timeline for the main geologic processes in this region. We inspected all the floor units of the paleolakes and excluded those heavily affected by continuous ejecta blankets, aeolian erosion, and undistinguishable modifications. In addition, paleolakes with small crater-counting areas (<100 km^2) were also excluded so that we can acquire absolute model ages with clear geologic significance and relatively small uncertainties. Finally, absolute model ages were obtained in 16 paleolakes. Their dated areas and plots are shown in Table S1, and the dating results are shown in Table 2. It can be seen that the sedimentary units have absolute model ages between 3.54 and 3.64 Ga, and this range extends to 3.44–

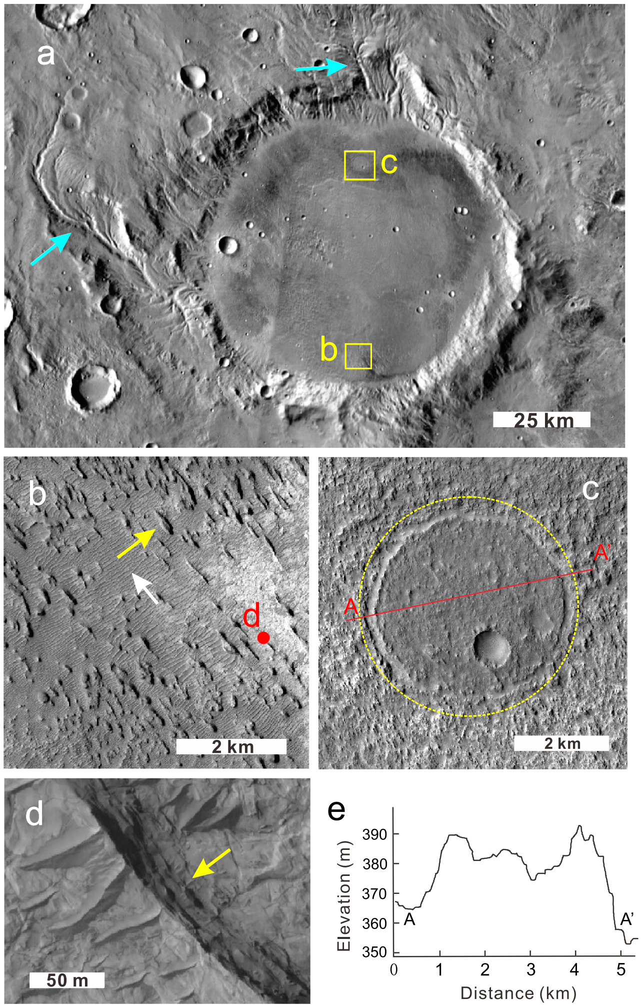

Figure 10. Aeolian resurfacing in paleolake No. 48. (a) THEMIS daytime IR mosaics of the paleolake No. 48 (Central coordinates: 59.18°E, 18.80°S). The cyan arrows point to the inlet valleys. Boxes show the location of (b) and (c); (b) linear dunes (indicated by the white arrow) and yardangs (indicated by the yellow arrow) on the southern basin floor. The red point indicates the location of (d); (c) a topographically inverted crater on the northern basin floor. The line AA′ indicates the location of the elevation profile in (e); (d) a HiRISE image shows the exposed layers (indicated by the yellow arrow) in the yardang field; (e) the elevation profile along the AA′ in (c) (HRSC/MOLA-blended DEM). CTX ID: P02_001834_1605_XI_19S300W. HiRISE ID: PSP_001834_1605_RED.

3.68 Ga when considering the error ranges. The absolute model ages of volcanic units are at 3.29–3.38 Ga (or 2.69–3.48 Ga considering the error ranges). Most of the dated glacial units show ages around 0.9 Ga, but the age of ~1.35 Ga was also acquired in one paleolake (No. 15). In addition, one unit in paleolake No. 17 could have experienced partial resurfacing processes, which results in two absolute model ages. There is an obvious "kink" at the diameter of 500 m in the size-frequency curve (Table S1), indicating a partial resurfacing event that erased the craters smaller than 500 m but left the craters with larger diameters. We acquired an absolute model age of ~3.33 Ga with craters larger than 600 m and also got the age of the resurfacing event (~1.36 Ga) by applying the resurfacing correction method (Michael & Neukum, 2010) to the smaller craters. Combining the surface morphology of the unit, it could be inferred that the age of ~1.36 Ga represents the glacial resurfacing event that also affected paleolake No. 15, while the older age (~3.33 Ga) represents the volcanic event that occurred in our study region, which is generally consistent with the dating results of other volcanic units.

3.5. Aqueous Mineral Identification

Aqueous minerals are important indicators for paleoclimate and hydroenvironment. Previous studies have shown that the northwestern Hellas region is an area with high concentrations of aqueous minerals such as phyllosilicates, chlorides, sulfates, and carbonates (Osterloo et al., 2010; Carter et al., 2013; Ehlmann & Edwards, 2014; Wray et al., 2016; Salese et al., 2016). In this study, we checked all the available CRISM targeted observation data overlapping the paleolakes to search for aqueous minerals. We further confirmed the specific mineral types in the previously proposed sites of aqueous minerals and discovered several new outcrops (Figure 11 and Table 3).

Our results (Table 3) show that phyllosilicates were identified in 10 paleolakes, and most of them are Fe/Mg-phyllosilicates (nontronite/saponite/vermiculite), which have diagnostic absorptions near 1.4, 1.9, and 2.3 μm. In addition, sporadic Al-smectites with absorptions near 1.4, 1.9, and 2.2 μm occur in paleolake No. 14 and overlie thick layers of Mg-smectite (Figures 12a and 12b). These phyllosilicates are distributed in both the "highland region" and "slope region," and they are found in erosional windows (Figure 12a) or near/on the rim of paleolake basins (Figure 12c). For the latter geologic setting, olivine is usually found associated with the phyllosilicates. For example, Fe-smectites were identified in the southeast rim of paleolake No. 39 (Figures 12c and 12d). They are distributed along the crest of the basin rim and associated with high concentration of olivine signatures.

Chlorides have a red slope with no obvious absorptions in the 1- to 2.6-μm wavelength range covered by CRISM and are not easily confirmed only based on CRISM data (Glotch et al., 2010; Osterloo et al., 2010). However, between 8 and 12 μm, which is covered by THEMIS data, chloride deposits exhibit a unique blue spectral slope. Therefore, we mainly used THEMIS data to search for chlorides as introduced in section 2.3. Chlorides were newly discovered on the floor of paleolake No. 31 (Figure 13). The deposit appears blue in THEMIS DCS 8-7-5 composites (Figure 13c) and green in THEMIS DCS 9-6-4 composites (Figure 13d). In addition, it shows a blue slope in THEMIS spectra (Figure 13e). We also made a detailed observation of the surface characteristics with CTX images and found the chloride-bearing area has a rough surface and a light tone (Figure 13b). In addition, the ejecta from craters as small as 140 m in diameters in this area show no features associated with chlorides in either CTX imagery or THEMIS DCS composites (Figures 13b–13d),

Table 2
Dating Results of the Paleolakes

Paleolake No.	Type of unit	Crater counting area (km^2)	Counted craters	N(1) (km^{-2})	Absolute model age (Ga)
1	Glacial	101.80	35	4.47×10^{-4}	0.917 (+0.15/−0.15)
6	Glacial	253.44	52	4.33×10^{-4}	0.889 (+0.12/−0.12)
8	Glacial	266.72	17	4.60×10^{-4}	0.943 (+0.23/−0.23)
10	Glacial	143.05	18	4.22×10^{-4}	0.866 (+0.20/−0.20)
15	Glacial	203.06	39	6.56×10^{-4}	1.35 (+0.21/−0.21)
17	Volcanic	892.73	7	1.97×10^{-3}	3.33 (+0.14/−0.64)
	Glacial		79	6.65×10^{-4}	1.36 (+0.14/−0.14)
24	Volcanic	442.62	14	2.01×10^{-3}	3.35 (+0.12/−0.37)
28	Volcanic	1143.86	22	1.94×10^{-3}	3.32 (+0.11/−0.27)
45	Volcanic	1203.44	23	2.09×10^{-3}	3.37 (+0.09/−0.19)
48	Volcanic	1259.00	18	1.87×10^{-3}	3.29 (+0.12/−0.35)
52	Volcanic	233.40	16	2.13×10^{-3}	3.38 (+0.10/−0.24)
39	Volcanic	801.06	33	1.88×10^{-3}	3.30 (+0.10/−0.23)
	Sedimentary	580.55	22	4.43×10^{-3}	3.63 (+0.04/−0.06)
31	Sedimentary	100.18	22	3.16×10^{-3}	3.54 (+0.05/−0.08)
36	Sedimentary	153.41	17	3.35×10^{-3}	3.56 (+0.06/−0.09)
37	Sedimentary	412.61	16	4.35×10^{-3}	3.62 (+0.05/−0.07)
40	Sedimentary	943.88	24	4.58×10^{-3}	3.64 (+0.04/−0.06)

suggesting it is a thin unit. Based on the excavation depth to crater diameter relation proposed by Baratoux et al. (2007),

$$H_{ex} = 0.109D^{0.872},$$

where H_{ex} and D represent excavation depth and crater diameter, respectively, we can acquire an excavation depth of ~20 m for the 140-m crater, which indicates the chloride-bearing materials are only distributed on the surface layer (less than 20 m) of the basin floor.

4. Discussion

4.1. Distribution and Morphology of the Paleolakes: Implication for Hydrologic Cycle

The distribution of the paleolakes shows obvious zonality. Open-basin lakes tend to have a higher concentration along the discontinuous scarp (−600 to 700 m) northwest of Hellas (Figure 2). Their distributions appear to be largely affected by topography, as they tend to occur in areas of larger topographic relief. A similar distribution has also been observed at global scales, in which open-basin lakes are extensively distributed near the dichotomy of Mars (Fassett & Head, 2008b; Goudge, Head, et al., 2012). The density distribution of the paleolakes exhibits a relatively large difference between the "highland region" and the southeast "slope region." The lower density of paleolakes in the "slope region," combined with the sparse distributed valleys

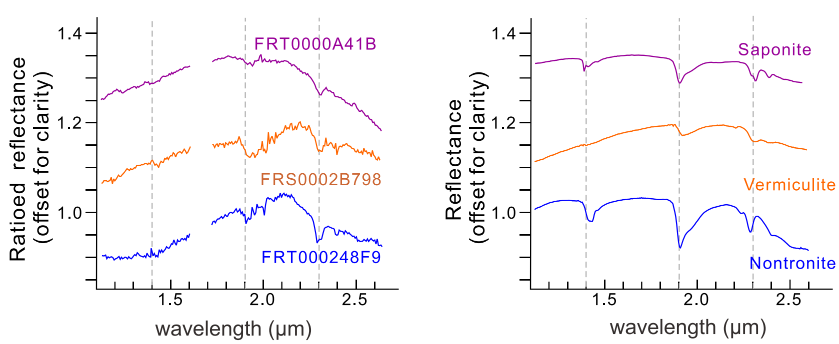

Figure 11. CRISM ratioed spectra of the newly identified phyllosilicates (left) and their best-match laboratory spectra from the USGS mineral spectra library (right).

Table 3
Results of Aqueous Mineral Identification in the Paleolakes

Paleolake No.	CRISM ID	Mineral type	Geologic setting	Reference
7	FRT0000A41B	Mg-smectite	Basin rim	This work
8	FRT00012D79	Fe-smectite	Erosional Window	Carter et al., 2013
14	HRS0000B703	Mg-smectite	Erosional	Carter et al., 2013
	FRT0001D977	Mg-smectite	Window	Carter et al., 2013
	/FRT0001ECBF	Al-smectite &		Carter et al., 2015
	FRT0000920A	Mg-smectite		Salese et al., 2016
19	FRT0000C37B	Mg-smectite	Erosional	Carter et al., 2013
	FRT00008D9E	Mg-smectite	Window	Carter et al., 2013
	FRS000272B1	Mg-smectite		Carter et al., 2013
	FRT00012BDA	Mg-smectite		Carter et al., 2013
20	FRS0002B798	Vermiculite	Erosional Window	This work
23	FRT0001689A	Mg-smectite	Erosional Window	Carter et al., 2013
24	FRT0000C7A1	Mg-smectite	Basin rim	Carter et al., 2013
31	THEMIS	Chloride	Basin floor	This work
37	FRT000248F9	Fe-smectite	Basin rim	This work
39	FRT0001279E	Fe-smectite	Basin rim	Carter et al., 2013
45	FRT00011D18	Vermiculite	Basin rim	Carter et al., 2013

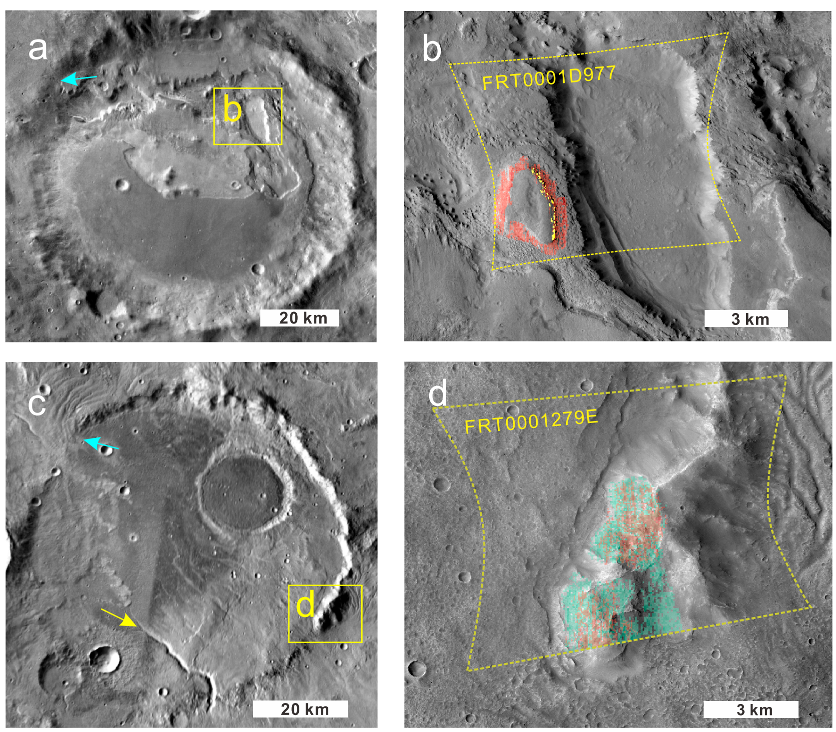

Figure 12. Representative geological settings of the identified phyllosilicates. (a) THEMIS mosaics of the paleolake No. 14 where phyllosilicates occur in an erosional window. The cyan arrow points to the inlet valley. The yellow box indicates the location of (b); (b) distribution of Mg-smectite (red) and Al-smectite (yellow) identified in CRISM data FRT0001D977. The yellow dashed line denotes the CRISM footprint. The background is CTX image (ID: G07_020835_1514_XN_28S303W); (c) THEMIS mosaics of the paleolake No. 39 where phyllosilicates exist on the crater rim. Cyan and yellow arrows point to the inlet and outlet valley, respectively. The yellow box shows the location of (d); (d) distribution of Mg-smectite (red) and olivine (green) identified in CRISM data FRT0001279E. The yellow dashed line denotes the CRISM footprint. The background is CTX image (ID: B09_012989_1585_XN_21S298W).

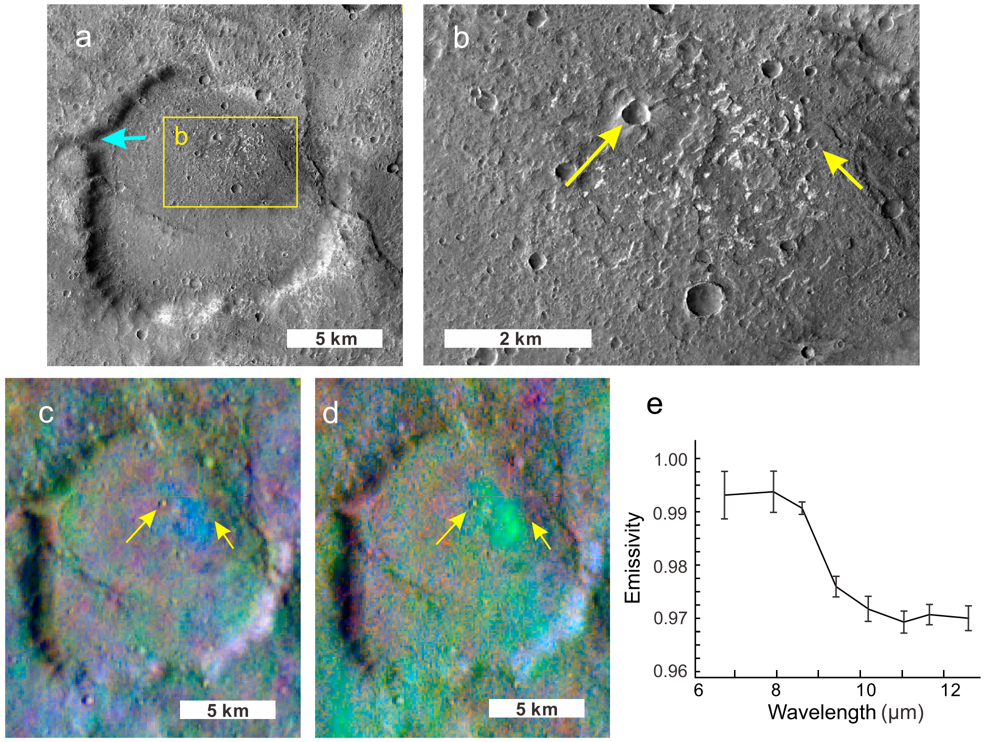

Figure 13. Identification of chlorides in paleolake No. 31. (a) CTX image of the paleolake No. 31. The blue arrow points to the inlet valley. The yellow box indicates the location of (b); (b) zoom of the area in (a) shows the surface details of the chloride-bearing region. The yellow arrows in this figure and also in (c)–(d) indicate the craters whose ejecta show no chloride characteristics; (c) THEMIS decorrelation stretch image of the paleolake No. 31 using band 8-7-5. The blueish color indicates the location of chlorides; (d) THEMIS decorrelation stretch image of the paleolake No. 31 using band 9-6-4. The greenish color indicates the location of chlorides; (e) average THEMIS surface emissivity spectra of the identified chloride-bearing deposits. CTX ID: B11_013741_1579_XN_22S309W. THEMIS ID: I50707002.

based on previous maps (e.g., Alemanno et al., 2018; Luo & Stepinski, 2009), may indicate that the "slope region" may have been partially covered by water due to the existence of a large lake or ocean in the Hellas basin that has been proposed by previous studies (Figure 14) (e.g., Bernhardt et al., 2016; Crown et al., 2005; Moore & Wilhelms, 2001; Salese et al., 2016; Wilson et al., 2007). The "Hellas Ocean" could have formed after the formation of the Hellas basin in a warm and wet climate, and then the water level decreased when the climate became drier. The "slope region" was largely exposed, and several closed-basin lakes, small open-basin lakes, and a small number of valleys developed in a transitional, semi-arid period from warm and wet conditions before the climate became too cold and dry to support liquid water at the surface.

The climate condition is also indicated by the morphology and types of paleolakes. Open-basin lakes usually indicate a longer duration of lake activity as sustained accumulation of water in the basin is needed to breach the crater rim and form outlet valleys (Fassett & Head, 2008b). In contrast, it is difficult to determine whether and how long a lake existed for a closed-basin lake. In our study region, about 77% of the paleolakes are closed-basin lakes, much higher than the percentage of closed-basin lakes at global scales (~48 % according to Goudge, Aureli, et al., 2015), which could be due to a semi-arid paleoclimate.

4.2. Sedimentary Landforms in the Paleolakes: Indication of Water Carrying Ability

Deltas/alluvial fans in the study region are concentrated along the discontinuous scarp and more than half of them are fan-like or lobate with a small area that usually indicates a limited water supply (Cabrol & Grin, 2001). Elongated fans could be formed by high discharge rates (Cabrol & Grin, 2001, 2002); however, their relatively small areas and lack of hydrated minerals indicate rapid formation with flood water release (de Villiers et al., 2013). This is most consistent with a semi-arid climate with short-term heavy precipitation (Harvey et al., 2005; Hooke, 1967).

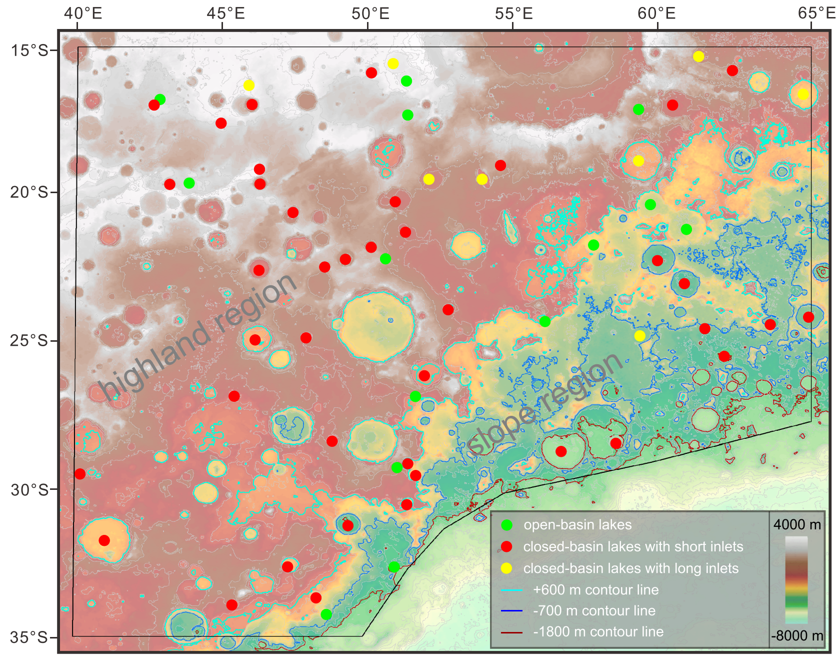

Figure 14. Topographic map of the study region showing the locations of the identified paleolakes and putative stands of water for the "Hellas Ocean" proposed by Wilson et al. (2007) (+700 and −600 m) and Crown et al. (2005) (−1,800 m). The background is colorized HRSC/MOLA-blended DEM.

Layered deposits are widely distributed in the paleolake basins. Previous studies have proposed an origin of deposition in a subaqueous environment for the layered deposits in the erosional windows (Ansan et al., 2011; Salese et al., 2016). The vertical profile of the layered deposits in paleolake No. 7 (Figure 7) illustrates a structure of light-toned thin layers (less than 1 m) with fine materials (Layered Unit 2) overlain by medium-toned thick layers (3–5 m) with coarse materials (Layered Unit 1). The total sedimentary packages are about 600 m in thickness. Similar layered structures were also found in other erosional windows, for example, paleolake No. 14 (Figure 6a). On the Earth, grain sizes of lake deposits can reflect the hydrodynamic condition (Leeder, 2009; Stow, 2005). Fine-grained deposits indicate a weak carrying capacity, especially in a deep-water environment, while coarse grains usually represent a high-energy environment in the near-shore area. On Mars, in our study region, the transition from a fine-grained lower unit to the coarse-grained upper unit could be due to the decrease of water depth and surface area of the lake induced by a climate change from wet to more arid conditions, which is consistent with the climate transition indicated by the distribution and types of the paleolakes detailed in section 4.1. Besides, several indurated interlayers with surficial cracks were observed in the Layered Unit 1 (Figures 7e and 7f), which may indicate slight climate change in a semi-arid climate.

4.3. Origin and Implications of the Aqueous Minerals

Analyses of the geological context and origin of aqueous minerals are important for the evaluation of paleoclimate. In the paleolakes of northwest Hellas, phyllosilicates are the most widely distributed aqueous minerals. Most of the phyllosilicates are Fe/Mg-smectites, but Al-smectites and vermiculites are also likely present. These clay minerals have different geologic settings. In five paleolakes, phyllosilicates were identified on the rim of paleolake basins and are always associated with olivine. The rim of a paleolake basin contains materials excavated by the impact event from the depth, which is supported by the existence of olivine. Ehlmann et al. (2011) assigned phyllosilicates with similar geologic context as "crustal," which are formed in the impact events or excavated from the subsurface. Therefore, this type of phyllosilicate deposit cannot be used to estimate the paleoclimate when the lakes were active as they formed before the lakes. In addition, olivine is easily altered to serpentine in wet and warm environments (Bristow & Milliken, 2011). The discovery of olivine and lack of serpentine may indicate that the paleoclimate was relatively dry or that the warm and wet climate did not last for a long time. However, it should be noted that olivine usually occurs on crater rims that have larger slopes and could be exposed after the period of wet climate by mass wasting or aeolian erosion. In this situation, it is unreliable to regard olivine as an indicator of dry climate.

Other phyllosilicates identified in this study occur in the layered deposits in erosional windows. Previous studies of the paleolakes found that phyllosilicates in similar settings are mostly detrital origin and were transported into the paleolakes through the connected valleys or from the basin rim rather than formed in situ (Ehlmann et al., 2011; Goudge, Head, et al., 2012; Wordsworth, 2016). The phyllosilicates identified in the intercrater plains of the northwest Hellas region (Carter et al., 2013; Salese et al., 2016) could be the source of the phyllosilicates in erosional windows. However, the origin of in situ weathering could not be excluded. We found that phyllosilicates in the erosional windows of the paleolakes in "slope region" are mostly Mg-smectites that are usually formed in a marginal marine environment (Bristow & Milliken, 2011). This further supports the existence of the "Hellas Ocean." A special case is that in the erosional window of the paleolake No. 14, sedimentary layers with Al-smectites overlying Mg-smectites were identified (Figure 12b), which has been considered as a weathering sequence by Carter et al. (2015). However, the distribution of Al-smectites is very limited and some of them are mixed with the Mg-smectites, which are typically formed in a relatively dry climate with limited rainfall (Carter et al., 2015). As this weathering profile is located near the top of the layered deposits, it may indicate a semi-arid climate in the terminal stage of the lacustrine activity.

Chlorides have been identified throughout the Martian surface by Osterloo et al. (2008, 2010). They found that chloride-bearing deposits usually occur in local lows in intercrater plains or in crater floors and proposed that most of the deposits may be formed by the evaporation of ponded brines, though efflorescence, and that impact and volcanic processes could also be possible formation mechanisms for some of the deposits (Osterloo et al., 2008). The chloride-bearing materials newly identified in our study are only present in the surface layer of a paleolake basin floor. This is inconsistent with a hydrothermal origin by impact or volcanic activity (Osterloo et al., 2010). Besides, no lava flows or volcanic edifices are present within or near the lake basin, which also does not support a volcanic origin. After eliminating the hypotheses above, we propose that efflorescence via atmospheric interactions or evaporation could be the possible formation mechanisms of the chlorides. Our results show that evaporites are rare in the paleolake basins in northwest Hellas. Previous studies of intercrater plains of this region have also found few evaporite outcrops (Salese et al., 2016). This could be caused by limited water input of the paleolakes and short duration of the lacustrine activity due to a semi-arid climate. Under this condition, there was not enough accumulation of dissolved ions to form the evaporites (Goudge, Head, et al., 2012).

4.4. Geologic and Climatic Histories of the Northwest Hellas Region

Our study of the geomorphology, mineralogy, and age of the paleolakes northwest of Hellas has depicted complicated geologic and climatic histories of the region.

The foremost event shaping of this region is the formation of Hellas basin at 4.0–4.1 Ga ago (Bottke & Andrews-Hanna, 2017; Frey, 2008; Werner, 2008). Impact ejecta and materials excavated from depth scattered in the study region. Soon after, some large craters were formed around the Hellas basin and acted as regional proto-basins. In addition, these impacts excavated phyllosilicates formed in the subsurface, likely by hydrothermal processes. At this time, there could have been a wet and warm climate so that large amounts of water accumulated in the Hellas basin and formed the "Hellas Ocean" that also covered the low-elevation area of the "slope region." Then, in the middle to late Noachian, the climate became drier although short-term heavy precipitation still may have occurred. The water level of the "Hellas Ocean" decreased and exposed the southeast low-elevation area where several closed-basin lakes and small valleys developed afterward.

Then, in the early Hesperian, the climate became cold and dry and the paleolakes gradually became inactive. At around 3.3 Ga, lava filled some of the paleolake basins and fully or partially covered the original lake deposits. This is consistent with the results from the dating of volcanic units in intercrater plains of the northwest Hellas region (Salese et al., 2016). However, considering the error ranges of the dating results, it is also possible that the draining of the paleolakes is contemporary with the volcanic activity.

In the Amazonian, aeolian process continued modifying the surface of basin floors and formed aeolian features such as yardangs and dunes. This area has also been influenced by several glacial periods in the

Amazonian due to the variation in the obliquity of Mars' rotation axis, but around 900 Ma, one of the largest glacial events happened in the region south of 25°S and led to the formation of various landforms related to glacial activity in the paleolakes such as softened terrains, ring-mold craters, and glacial-like deposits.

The climatic history of the study area reveals the complexity of Martian climate. Although different models of Martian climate have been proposed (e.g., Craddock & Howard, 2002; Haberle, 1998; Head & Marchant, 2014; Ramirez & Craddock, 2018; Wordsworth, 2016), regional variation of the climate is still poorly understood. The northwest Hellas region shows a climate change from warm and wet to semi-arid in the Noachian and then to cold and dry in the Hesperian. This work provides more detail for the transition process of Martian regional climate from Noachian to Hesperian in this region. However, as our work is limited in the northwest Hellas region, more studies are still needed to better clarify the characteristics and mechanism of Martian climate change at regional scales.

5. Conclusions

A detailed investigation of paleolake basins has been carried out in the northwest Hellas region with high-resolution image and topographic and spectral data. We have the following conclusions:

We identified a total of 64 paleolakes; 49 of which were newly reported. The basic hydrologic parameters for each paleolake were obtained, and their distribution was studied.

Sedimentary landforms including delta/alluvial fans and layered deposits were identified. The delta/alluvial fans are relatively small in area and can be divided into three types. Layered deposits are well exposed in eight erosional windows and exhibit two units with different layer characteristics.

Extensive volcanic resurfacing of the paleolakes peaked around 3.3 Ga, which could be contemporary or slightly later than the draining of the paleolakes. Then, around 900 Ma, one of the largest glacial events in this region resurfaced some of the paleolakes south of 25°S.

Aqueous minerals including phyllosilicates and chlorides were identified in the paleolakes. The phyllosilicates with different geologic settings may have different origins. Chlorides were probably formed by evaporation or efflorescence via atmospheric interactions.

Our study provided new insights into the geologic and climatic histories of the region and revealed regional variation of Martian climate that is still needed to clarify. The northwest Hellas region may have undergone a transitional, semi-arid period from warm and wet conditions in the Noachian before the climate became too cold and dry to support surface liquid water in the early Hesperian. In the Late Hesperian and Amazonian, volcanic and glacial events resurfaced the floor of lake basins, respectively.

Acknowledgments

We thank the Editor-in-Chief Laurent Montesi, the Associate Editor Caleb Fassett, and two anonymous reviewers for their reviews that greatly improved the manuscript. We also thank Deanne Rogers and Jun Huang for their assistance in data processing. This study was supported by the Natural Science Foundation of China (41830214), China Postdoctoral Science Foundation (2018M630889), the Pre-research Project on Civil Aerospace Technologies (D020101) of CNSA, and the Science and Technology Development Fund, Macau SAR. All the remote-sensing data used can be accessed from JMARS (https://jmars.mars.asu.edu/) and Planetary Data System (https://pds-geosciences.wustl.edu/). The crater counting files and the original ratioed spectra for the newly identified aqueous minerals are available in the in-text data citation reference: Zhao (2020).

References

Alemanno, G., Orofino, V., & Mancarella, F. (2018). Global map of Martian fluvial systems: Age and total eroded volume estimations. *Earth and Space Science*, *5*(10), 560–577. https://doi.org/10.1029/2018ea000362

Ansan, V., Loizeau, D., Mangold, N., Le Mouélic, S., Carter, J., Poulet, F., et al. (2011). Stratigraphy, mineralogy, and origin of layered deposits inside Terby crater, Mars. *Icarus*, *211*(1), 273–304. https://doi.org/10.1016/j.icarus.2010.09.011

Baker, V. R. (1978). The spokane flood controversy and the Martian outflow channels. *Science*, *202*(4374), 1249–1256. https://doi.org/10.1126/science.202.4374.1249

Baker, V. R. (2006). Geomorphological evidence for water on Mars. *Elements*, *2*(3), 139–143. https://doi.org/10.2113/gselements.2.3.139

Bandfield, J. L. (2004). Atmospheric correction and surface spectral unit mapping using Thermal Emission Imaging System data. *Journal of Geophysical Research*, *109*(E10), E10008. https://doi.org/10.1029/2004je002289

Baratoux, D., Pinet, P., Gendrin, A., Kanner, L., Mustard, J., Daydou, Y., et al. (2007). Mineralogical structure of the subsurface of Syrtis Major from OMEGA observations of lobate ejecta blankets. *Journal of Geophysical Research: Planets*, *112*(E8), E08S05. https://doi.org/10.1029/2007JE002890

Bernhardt, H., Hiesinger, H., Ivanov, M. A., Ruesch, O., Erkeling, G., & Reiss, D. (2016). Photogeologic mapping and the geologic history of the Hellas basin floor, Mars. *Icarus*, *264*, 407–442. https://doi.org/10.1016/j.icarus.2015.09.031

Bottke, W. F., & Andrews-Hanna, J. C. (2017). A post-accretionary lull in large impacts on early Mars. *Nature Geoscience*, *10*(5), 344–348. https://doi.org/10.1038/ngeo2937

Bristow, T. F., & Milliken, R. E. (2011). Terrestrial perspective on authigenic clay mineral production in ancient Martian lakes. *Clays and Clay Minerals*, *59*(4), 339–358. https://doi.org/10.1346/ccmn.2011.0590401

Cabrol, N. A., & Grin, E. A. (1999). Distribution, classification, and ages of Martian impact crater lakes. *Icarus*, *142*(1), 160–172. https://doi.org/10.1006/icar.2000.6530

Cabrol, N. A., & Grin, E. A. (2001). The Evolution of Lacustrine Environments on Mars: Is Mars Only Hydrologically Dormant? *Icarus*, *149*(2), 291–328. https://doi.org/10.1006/icar.2000.6530

Cabrol, N. A., & Grin, E. A. (2002). Overview on the formation of paleolakes and ponds on Mars. *Global and Planetary Change*, *35*(3), 199–219. https://doi.org/10.1016/S0921-8181(02)00127-3

Cabrol, N. A., Grin, E. A., Newsom, H. E., Landheim, R., & McKay, C. P. (1999). Hydrogeologic evolution of Gale crater and its relevance to the exobiological exploration of Mars. *Icarus*, *139*(2), 235–245.

Carr, M. H. (1995). The Martian drainage system and the origin of valley networks and fretted channels. *Journal of Geophysical Research: Planets*, *100*(E4), 7479–7507.

Carter, J., Loizeau, D., Mangold, N., Poulet, F., & Bibring, J.-P. (2015). Widespread surface weathering on early Mars: A case for a warmer and wetter climate. *Icarus*, *248*, 373–382. https://doi.org/10.1016/j.icarus.2014.11.011

Carter, J., Poulet, F., Bibring, J. P., Mangold, N., & Murchie, S. (2013). Hydrous minerals on Mars as seen by the CRISM and OMEGA imaging spectrometers: Updated global view. *Journal of Geophysical Research: Planets*, *118*, 831–858. https://doi.org/10.1029/2012je004145

Cawley, J. C., & Irwin, R. P. (2018). Evolution of escarpments, pediments, and plains in the Noachian highlands of Mars. *Journal of Geophysical Research: Planets*, *123*(12), 3167–3187. https://doi.org/10.1029/2018je005681

Christensen, P. R., Jakosky, B. M., Kieffer, H. H., Malin, M. C., McSween, H. Y. Jr., Nealson, K., et al. (2004). The Thermal Emission Imaging System (THEMIS) for the Mars 2001 Odyssey Mission. *Space Science Reviews*, *110*(1/2), 85–130. https://doi.org/10.1023/b:spac.0000021008.16305.94

Cowart, J. C., Rogers, A. D., & Edwards, C. S. (2019). *Mapping and characterization of Martian intercrater bedrock plains: Insights into resurfacing processes in the Martian cratered highlands*, (p. 124). Journal of Geophysical Research: Planets. https://doi.org/10.1029/2019JE006062

Craddock, R. A., & Howard, A. D. (2002). The case for rainfall on a warm, wet early Mars. *Journal of Geophysical Research*, *107*(E11), 21-1–21-36. https://doi.org/10.1029/2001je001505

Crown, D. A., Bleamaster, L. F., & Mest, S. C. (2005). Styles and timing of volatile-driven activity in the eastern Hellas region of Mars. *Journal of Geophysical Research*, *110*(E12), E12S22. https://doi.org/10.1029/2005je002496

De Hon, R. (1992). Martian lake basins and lacustrine plains. *Earth, Moon, and Planets*, *56*(2), 95–122. https://doi.org/10.1007/BF00056352

de Villiers, G., Kleinhans, M. G., & Postma, G. (2013). Experimental delta formation in crater lakes and implications for interpretation of Martian deltas. *Journal of Geophysical Research: Planets*, *118*, 651–670. https://doi.org/10.1002/jgre.20069

Dehouck, E., Mangold, N., Le Mouélic, S., Ansan, V., & Poulet, F. (2010). Ismenius Cavus, Mars: A deep paleolake with phyllosilicate deposits. *Planetary and Space Science*, *58*(6), 941–946. https://doi.org/10.1016/j.pss.2010.02.005

Dickson, J. L., Head, J. W., & Marchant, D. R. (2010). Kilometer-thick ice accumulation and glaciation in the northern mid-latitudes of Mars: Evidence for crater-filling events in the Late Amazonian at the Phlegra Montes. *Earth and Planetary Science Letters*, *294*(3), 332–342.

Edwards, C. S., Bandfield, J. L., Christensen, P. R., & Rogers, A. D. (2014). The formation of infilled craters on Mars: Evidence for widespread impact induced decompression of the early martian mantle? *Icarus*, *228*, 149–166. https://doi.org/10.1016/j.icarus.2013.10.005

Ehlmann, B. L., & Edwards, C. S. (2014). Mineralogy of the Martian surface. *Annual Review of Earth and Planetary Sciences*, *42*(1), 291–315. https://doi.org/10.1146/annurev-earth-060313-055024

Ehlmann, B. L., Mustard, J. F., Murchie, S. L., Bibring, J. P., Meunier, A., Fraeman, A. A., et al. (2011). Subsurface water and clay mineral formation during the early history of Mars. *Nature*, *479*(7371), 53–60. https://doi.org/10.1038/nature10582

Eigenbrode, J. L., Summons, R. E., Steele, A., Freissinet, C., Millan, M., Navarro-González, R., et al. (2018). Organic matter preserved in 3-billion-year-old mudstones at Gale crater, Mars. *Science*, *360*(6393), 1096–1101. https://doi.org/10.1126/science.aas9185

Fassett, C. I. (2016). Analysis of impact crater populations and the geochronology of planetary surfaces in the inner solar system. *Journal of Geophysical Research: Planets*, *121*, 1900–1926. https://doi.org/10.1002/2016je005094

Fassett, C. I., & Head, J. W. (2005). Fluvial sedimentary deposits on Mars: Ancient deltas in a crater lake in the Nili Fossae region. *Geophysical Research Letters*, *32*, L14201. https://doi.org/10.1029/2005gl023456

Fassett, C. I., & Head, J. W. (2008a). The timing of Martian valley network activity: Constraints from buffered crater counting. *Icarus*, *195*(1), 61–89. https://doi.org/10.1016/j.icarus.2007.12.009

Fassett, C. I., & Head, J. W. (2008b). Valley network-fed, open-basin lakes on Mars: Distribution and implications for Noachian surface and subsurface hydrology. *Icarus*, *198*(1), 37–56. https://doi.org/10.1016/j.icarus.2008.06.016

Forsythe, R. D., & Blackwelder, C. R. (1998). Closed drainage crater basins of the Martian highlands: Constraints on the early Martian hydrologic cycle. *Journal of Geophysical Research*, *103*(E13), 31421–31431. https://doi.org/10.1029/98je01966

Frey, H. (2008). Ages of very large impact basins on Mars: Implications for the late heavy bombardment in the inner solar system. *Geophysical Research Letters*, *35*, L13203. https://doi.org/10.1029/2008gl033515

Fukushi, K., Sekine, Y., Sakuma, H., Morida, K., & Wordsworth, R. (2019). Semiarid climate and hyposaline lake on early Mars inferred from reconstructed water chemistry at Gale. *Nature Communications*, *10*(1), 4896. https://doi.org/10.1038/s41467-019-12871-6

Glotch, T. D., Bandfield, J. L., Tornabene, L. L., Jensen, H. B., & Seelos, F. P. (2010). Distribution and formation of chlorides and phyllosilicates in Terra Sirenum, Mars. *Geophysical Research Letters*, *37*, L16202. https://doi.org/10.1029/2010gl044557

Glotch, T. D., Bandfield, J. L., Wolff, M. J., Arnold, J. A., & Che, C. (2016). Constraints on the composition and particle size of chloride salt-bearing deposits on Mars. *Journal of Geophysical Research: Planets*, *121*, 454–471. https://doi.org/10.1002/2015je004921

Glotch, T. D., & Christensen, P. R. (2005). Geologic and mineralogic mapping of Aram Chaos: Evidence for a water-rich history. *Journal of Geophysical Research*, *110*(E9), E09006. https://doi.org/10.1029/2004je002389

Goldspiel, J. M., & Squyres, S. W. (1991). Ancient aqueous sedimentation on Mars. *Icarus*, *89*(2), 392–410. https://doi.org/10.1016/0019-1035(91)90186-W

Goudge, T. A., Aureli, K. L., Head, J. W., Fassett, C. I., & Mustard, J. F. (2015). Classification and analysis of candidate impact crater-hosted closed-basin lakes on Mars. *Icarus*, *260*, 346–367. https://doi.org/10.1016/j.icarus.2015.07.026

Goudge, T. A., Head, J. W., Mustard, J. F., & Fassett, C. I. (2012). An analysis of open-basin lake deposits on Mars: Evidence for the nature of associated lacustrine deposits and post-lacustrine modification processes. *Icarus*, *219*(1), 211–229. https://doi.org/10.1016/j.icarus.2012.02.027

Goudge, T. A., Milliken, R. E., Head, J. W., Mustard, J. F., & Fassett, C. I. (2017). Sedimentological evidence for a deltaic origin of the western fan deposit in Jezero crater, Mars and implications for future exploration. *Earth and Planetary Science Letters*, *458*, 357–365. https://doi.org/10.1016/j.epsl.2016.10.056

Goudge, T. A., Mohrig, D., Cardenas, B. T., Hughes, C. M., & Fassett, C. I. (2018). Stratigraphy and paleohydrology of delta channel deposits, Jezero crater, Mars. *Icarus*, *301*, 58–75. https://doi.org/10.1016/j.icarus.2017.09.034

Goudge, T. A., Mustard, J. F., Head, J. W., & Fassett, C. I. (2012). Constraints on the history of open-basin lakes on Mars from the composition and timing of volcanic resurfacing. *Journal of Geophysical Research: Planets*, *117*, E00J21. https://doi.org/10.1029/2012je004115

Goudge, T. A., Mustard, J. F., Head, J. W., Fassett, C. I., & Wiseman, S. M. (2015). Assessing the mineralogy of the watershed and fan deposits of the Jezero crater paleolake system, Mars. *Journal of Geophysical Research: Planets*, *120*, 775–808.

Grant, J. A., Golombek, M. P., Wilson, S. A., Farley, K. A., Williford, K. H., & Chen, A. (2018). The science process for selecting the landing site for the 2020 Mars rover. *Planetary and Space Science*, *164*, 106–126.

Cabrol, N. A, & Grin, E. A. (2001). The evolution of lacustrine environments on Mars: Is Mars only hydrologically dormant?. *Icarus*, *149*(2), 291-328. https://doi.org/10.1006/icar.2000.6530.

Grin, E. A., & Cabrol, N. A. (1997). Limnologic analysis of Gusev crater paleolake, Mars. *Icarus*, *130*(2), 461–474. https://doi.org/10.1006/icar.1997.5817

Grotzinger, J. P., Gupta, S., Malin, M. C., Rubin, D. M., Schieber, J., Siebach, K., et al. (2015). Deposition, exhumation, and paleoclimate of an ancient lake deposit. Gale crater, Mars. *Science*, *350*(6257), aac7575. https://doi.org/10.1126/science.aac7575

Gulick, V. C., & Baker, V. R. (1989). Fluvial valleys and Martian palaeoclimates. *Nature*, *341*(6242), 514–516. https://doi.org/10.1038/341514a0

Haberle, R. M. (1998). Early Mars climate models. *Journal of Geophysical Research: Planets*, *103*(E12), 28467–28479. https://doi.org/10.1029/98je01396

Hartmann, W. K., & Neukum, G. (2001). Cratering chronology and the evolution of Mars. *Space Science Reviews*, *96*, 165–194. https://doi.org/10.1007/978-94-017-1035-0_6

Harvey, A. M., Mather, A. E., & Stokes, M. (2005). Alluvial fans: Geomorphology, sedimentology, dynamics—Introduction. A review of alluvial-fan research. *Geological Society, London, Special Publications*, *251*(1), 1–7.

Haskin, L. A., Wang, A., Jolliff, B. L., McSween, H. Y., Clark, B. C., Des Marais, D. J., et al. (2005). Water alteration of rocks and soils on Mars at the Spirit rover site in Gusev crater. *Nature*, *436*(7047), 66–69. https://doi.org/10.1038/nature03640

Head, J. W., & Marchant, D. R. (2014). The climate history of early Mars: Insights from the Antarctic McMurdo Dry Valleys hydrologic system. *Antarctic Science*, *26*(06), 774–800.

Hooke, R. L. (1967). Processes on arid-region alluvial fans. *The Journal of Geology*, *75*(4), 438–460. https://doi.org/10.1086/627271

Irwin, R. P., Howard, A. D., Craddock, R. A., & Moore, J. M. (2005). An intense terminal epoch of widespread fluvial activity on early Mars: 2. Increased runoff and paleolake development. *Journal of Geophysical Research*, *110*(E12), E12S15. https://doi.org/10.1029/2005je002460

Irwin, R. P., Lewis, K. W., Howard, A. D., & Grant, J. A. (2015). Paleohydrology of Eberswalde crater, Mar. *Geomorphology*, *240*, 83–101.

Irwin, R. P., Maxwell, T. A., Howard, A. D., Craddock, R. A., & Leverington, D. W. (2002). A large paleolake basin at the head of Ma'adim Vallis. *Mars, Science*, *296*(5576), 2209–2212.

Irwin, R. P., Tooth, S., Craddock, R. A., Howard, A. D., & de Latour, A. B. (2014). Origin and development of theater-headed valleys in the Atacama Desert, northern Chile: Morphological analogs to Martian valley networks. *Icarus*, *243*, 296–310. https://doi.org/10.1016/j.icarus.2014.08.012

Irwin, R. P., Wray, J. J., Mest, S. C., & Maxwell, T. A. (2018). Wind-eroded crater floors and intercrater plains, Terra Sabaea, Mars. *Journal of Geophysical Research: Planets*, *123*(2), 445–467. https://doi.org/10.1002/2017je005270

Kraal, E. R., van Dijk, M., Postma, G., & Kleinhans, M. G. (2008). Martian stepped-delta formation by rapid water release. *Nature*, *451*(7181), 973–976. https://doi.org/10.1038/nature06615

Kress, A. M., & Head, J. W. (2008). Ring-mold craters in lineated valley fill and lobate debris aprons on Mars: Evidence for subsurface glacial ice. *Geophysical Research Letters*, *35*(23), L23206.

Leeder, M. R. (2009). *Sedimentology and sedimentary basins: From turbulence to tectonics*. Chichester, West Sussex, UK: John Wiley & Sons.

Leonard, G. J., & Tanaka, K. L. (2001). *Geologic map of the Hellas region of Mars*. US Geological Survey: US Department of the Interior.

Leverington, D., & Maxwell, T. (2004). An igneous origin for features of a candidate crater-lake system in western Memnonia, Mars. *Journal of Geophysical Research*, *109*(E6), E06006. https://doi.org/10.1029/2004je002237

Leverington, D. W. (2006). Volcanic processes as alternative mechanisms of landform development at a candidate crater-lake site near Tyrrhena Patera, Mars. *Journal of Geophysical Research*, *111*(E11), E11002. https://doi.org/10.1029/2004je002382

Levy, J., Head, J. W., & Marchant, D. R. (2010). Concentric crater fill in the northern mid-latitudes of Mars: Formation processes and relationships to similar landforms of glacial origin. *Icarus*, *209*(2), 390–404. https://doi.org/10.1016/j.icarus.2010.03.036

Li, H., Robinson, M., & Jurdy, D. (2005). Origin of Martian northern hemisphere mid-latitude lobate debris aprons. *Icarus*, *176*(2), 382–394. https://doi.org/10.1016/j.icarus.2005.02.011

Luo, W., & Stepinski, T. F. (2009). Computer-generated global map of valley networks on Mars. *Journal of Geophysical Research*, *114*(E11), E11010. https://doi.org/10.1029/2009je003357

McGuire, P. C., Bishop, J. L., Brown, A. J., Fraeman, A. A., Marzo, G. A., Morgan, M. F., et al. (2009). An improvement to the volcano-scan algorithm for atmospheric correction of CRISM and OMEGA spectral data. *Planetary and Space Science*, *57*(7), 809–815.

McSween, H. Y. (2006). Water on Mars. *Elements*, *2*(3), 135–137. https://doi.org/10.2113/gselements.2.3.135

Michael, G. G., & Neukum, G. (2010). Planetary surface dating from crater size–frequency distribution measurements: Partial resurfacing events and statistical age uncertainty. *Earth and Planetary Science Letters*, *294*(3-4), 223–229. https://doi.org/10.1016/j.epsl.2009.12.041

Michalski, J. R., Glotch, T. D., Rogers, A. D., Niles, P. B., Cuadros, J., Ashley, J. W., et al. (2019). The geology and astrobiology of McLaughlin Crater, Mars: An ancient Lacustrine Basin containing turbidites, mudstones, and serpentinites. *Journal of Geophysical Research: Planets*, *124*(4), 910–940. https://doi.org/10.1029/2018je005796

Milliken, R., Mustard, J., & Goldsby, D. (2003). Viscous flow features on the surface of Mars: Observations from high-resolution Mars Orbiter Camera (MOC) images. *Journal of Geophysical Research: Planets (1991–2012)*, *108*(E6), 211–227.

Moore, J., & Wilhelms, D. E. (2001). Hellas as a possible site of ancient ice-covered lakes on Mars. *Icarus*, *154*(2), 258–276. https://doi.org/10.1006/icar.2001.6736

Murchie, S., Arvidson, R., Bedini, P., Beisser, K., Bibring, J. P., Bishop, J., et al. (2007). Compact Reconnaissance Imaging Spectrometer for Mars (CRISM) on Mars Reconnaissance Orbiter (MRO). *Journal of Geophysical Research*, *112*(E5), E05S03. https://doi.org/10.1029/2006je002682

Mustard, J. F., Poulet, F., Head, J. W., Mangold, N., Bibring, J. P., Pelkey, S. M., et al. (2007). Mineralogy of the Nili Fossae region with OMEGA/Mars Express data: 1. Ancient impact melt in the Isidis Basin and implications for the transition from the Noachian to Hesperian. *Journal of Geophysical Research*, *112*(E8), E08S03. https://doi.org/10.1029/2006je002834

Neukum, G., Ivanov, B. A., & Hartmann, W. K. (2001). Cratering records in the inner solar system in relation to the lunar reference system. *Space Science Reviews*, *12*, 55–86. https://doi.org/10.1007/978-94-017-1035-0_3

Newsom, H. E., Brittelle, G. E., Hibbitts, C. A., Crossey, L. J., & Kudo, A. M. (1996). Impact crater lakes on Mars. *Journal of Geophysical Research*, *101*(E6), 14951. https://doi.org/10.1029/96je01139

Noe Dobrea, E., Bell, J., McConnochie, T., & Malin, M. (2006). Analysis of a spectrally unique deposit in the dissected Noachian terrain of Mars. *Journal of Geophysical Research: Planets*, *111*, E06007.

Osterloo, M., Hamilton, V., Bandfield, J., Glotch, T., Baldridge, A., Christensen, P., et al. (2008). Chloride-bearing materials in the southern highlands of Mars. *Science*, *319*(5870), 1651–1654. https://doi.org/10.1126/science.1150690

Osterloo, M. M., Anderson, F. S., Hamilton, V. E., & Hynek, B. M. (2010). Geologic context of proposed chloride-bearing materials on Mars. *Journal of Geophysical Research*, *115*(E10), E10012. https://doi.org/10.1029/2010je003613

Pajola, M., Rossato, S., Carter, J., Baratti, E., Pozzobon, R., & Erculiani, et al. (2016). Eridania Basin: An ancient paleolake floor as the next landing site for the Mars 2020 rover. *Icarus*, *275*, 163–182.

Palucis, M. C., Dietrich, W. E., Williams, R. M., Hayes, A. G., Parker, T., Sumner, D. Y., et al. (2016). Sequence and relative timing of large lakes in Gale crater (Mars) after the formation of Mount Sharp. *Journal of Geophysical Research: Planets*, *121*(3), 472–496.

Pathare, A., Joseph, E., Crown, D., Chuang, F., Berman, D., & Koutnik, M. (2017). *Glacial flow within Martian lobate debris aprons: Evidence from surface texture mapping in eastern Hellas. Paper presented at Lunar and Planetary Science Conference*. USA: Houston.

Pelkey, S. M., Mustard, J. F., Murchie, S., Clancy, R. T., Wolff, M., Smith, M., et al. (2007). CRISM multispectral summary products: Parameterizing mineral diversity on Mars from reflectance. *Journal of Geophysical Research*, *112*(E8), E08S14. https://doi.org/10.1029/2006je002831

Ramirez, R. M., & Craddock, R. A. (2018). The geological and climatological case for a warmer and wetter early Mars. *Nature Geoscience*, *11*(4), 230–237. https://doi.org/10.1038/s41561-018-0093-9

Rivera-Hernández, F., & Palucis, M. C. (2019). Do deltas along the crustal dichotomy boundary of Mars in the gale crater region record a northern ocean? *Geophysical Research Letters*, *46*(15), 8689–8699. https://doi.org/10.1029/2019gl083046

Rodriguez, J. A. P., Kargel, J. S., Baker, V. R., Gulick, V. C., Berman, D. C., Fairén, A. G., et al. (2015). Martian outflow channels: How did their source aquifers form, and why did they drain so rapidly? *Scientific Reports*, *5*, 13404.

Rogers, A. D., & Nazarian, A. H. (2013). Evidence for Noachian flood volcanism in Noachis Terra, Mars, and the possible role of Hellas impact basin tectonics. *Journal of Geophysical Research: Planets*, *118*, 1094–1113. https://doi.org/10.1002/jgre.20083

Rogers, A. D., Warner, N. H., Golombek, M. P., Head, J. W. 3rd, & Cowart, J. C. (2018). Areally extensive surface bedrock exposures on Mars: Many are clastic rocks, not lavas. *Geophysical Research Letters*, *45*, 1767–1777. https://doi.org/10.1002/2018GL077030

Salese, F., Ansan, V., Mangold, N., Carter, J., Ody, A., Poulet, F., et al. (2016). A sedimentary origin for intercrater plains north of the Hellas basin: Implications for climate conditions and erosion rates on early Mars. *Journal of Geophysical Research: Planets*, *121*(11), 2239–2267. https://doi.org/10.1002/2016je005039

Salvatore, M. R., Goudge, T. A., Bramble, M. S., Edwards, C. S., Bandfield, J. L., Amador, E., et al. (2018). Bulk mineralogy of the NE Syrtis and Jezero crater regions of Mars derived through thermal infrared spectral analyses. *Icarus*, *301*, 76–96. https://doi.org/10.1016/j.icarus.2017.09.019

Shean, D., Fahle, J., Malin, M., Edwards, L., & Posiolova, L. (2011). *MRO CTX stereo image processing and preliminary DEM quality assessment. Paper presented at Lunar and Planetary Science Conference*. USA: Houston.

Skilling, I. P. (2002). Basaltic pahoehoe lava-fed deltas: Large-scale characteristics, clast generation, emplacement processes and environmental discrimination. *Geological Society, London, Special Publications*, *202*(1), 91–113. https://doi.org/10.1144/gsl.Sp.2002.202.01.06

Squyres, S. W. (1979). The distribution of lobate debris aprons and similar flows on Mars. *Journal of Geophysical Research - Solid Earth*, *84*(B14), 8087–8096.

Squyres, S. W., Arvidson, R. E., Bollen, D., Bell, J. F., Brückner, J., Cabrol, N. A., et al. (2006). Overview of the opportunity Mars exploration rover mission to Meridiani Planum: Eagle crater to purgatory ripple. *Journal of Geophysical Research: Planets*, *111*, E12S12. https://doi.org/10.1029/2006je002771

Squyres, S. W., & Carr, M. H. (1986). Geomorphic evidence for the distribution of ground ice on Mars. *Science*, *231*(4735), 249–252. https://doi.org/10.1126/science.231.4735.249

Stow, D. A. (2005). *Sedimentary rocks in the field: A colour guide*. Burlington, MA: Academic Press.

Viviano-Beck, C. E., Seelos, F. P., Murchie, S. L., Kahn, E. G., Seelos, K. D., Taylor, H. W., et al. (2014). Revised CRISM spectral parameters and summary products based on the currently detected mineral diversity on Mars. *Journal of Geophysical Research: Planets*, *119*, 1403–1431. https://doi.org/10.1002/2014je004627

Warner, N., Gupta, S., Lin, S.-Y., Kim, J.-R., Muller, J.-P., & Morley, J. (2010). Late Noachian to Hesperian climate change on Mars: Evidence of episodic warming from transient crater lakes near Ares Vallis. *Journal of Geophysical Research*, *115*(E6), E06013. https://doi.org/10.1029/2009je003522

Werner, S. (2008). The early Martian evolution—Constraints from basin formation ages. *Icarus*, *195*(1), 45–60.

Wichman, R. W., & Schultz, P. H. (1989). Sequence and mechanisms of deformation around the Hellas and Isidis Impact Basins on Mars. *Journal of Geophysical Research*, *94*(B12), 17333. https://doi.org/10.1029/JB094iB12p17333

Wilson, S. A., Howard, A. D., Moore, J. M., & Grant, J. A. (2007). Geomorphic and stratigraphic analysis of Crater Terby and layered deposits north of Hellas basin, Mars. *Journal of Geophysical Research*, *112*(E8), 582–596. https://doi.org/10.1029/2006je002830

Wordsworth, R. D. (2016). The climate of early Mars. *Annual Review of Earth and Planetary Sciences*, *44*(1), 381–408. https://doi.org/10.1146/annurev-earth-060115-012355

Wray, J. J. (2012). Gale crater: The Mars Science Laboratory/Curiosity Rover Landing Site. *International Journal of Astrobiology*, *12*(01), 25–38. https://doi.org/10.1017/s1473550412000328

Wray, J. J., Murchie, S. L., Bishop, J. L., Ehlmann, B. L., Milliken, R. E., Wilhelm, M. B., et al. (2016). Orbital evidence for more widespread carbonate-bearing rocks on Mars. *Journal of Geophysical Research: Planets*, *121*, 652–677.

Zhao, Jiannan, 2020. "Data for: Paleolakes in the Northwest Hellas Region, Mars: Implications for the regional geologic history and paleoclimate", https://doi.org/10.7910/DVN/B8WEYT, Harvard Dataverse, V1